Agenzia nazionale per le nuove tecnologie,
l'energia e lo sviluppo economico sostenibile

MINISTERO DELLO SVILUPPO ECONOMICO

Ricerca di Sistema elettrico

Developing multiscale transient simulations with FEM-LCORE code

D. Cerroni, S. Manservisi, E. Vincenzi

Report RdS/2013/050

DEVELOPING MULTISCALE TRANSIENT SIMULATIONS WITH FEM-LCORE CODE

D. Cerroni, S. Manservisi, E. Vincenzi (UNIBO)

Settembre 2013

Report Ricerca di Sistema Elettrico

Accordo di Programma Ministero dello Sviluppo Economico - ENEA
Piano Annuale di Realizzazione 2012
Area: Produzione di energia elettrica e protezione dell'ambiente
Progetto: Sviluppo competenze scientifiche nel campo della sicurezza nucleare e collaborazione ai programmi internazionali per il nucleare di IV Generazione
Obiettivo: Sviluppo competenze scientifiche nel campo della sicurezza nucleare
Responsabile del Progetto: Mariano Tarantino, ENEA

Il presente documento descrive le attività di ricerca svolte all'interno dell'Accordo di collaborazione "Sviluppo competenze scientifiche nel campo della sicurezza nucleare e collaborazione ai programmi internazionali per il nucleare di IV generazione"
Responsabile scientifico ENEA: Mariano Tarantino
Responsabile scientifico CIRTEN: Giuseppe Forasassi

ENEA Ricerca Sistema Elettrico	Sigla di identificazione	Distrib.	Pag.	di
	ADPFISS – LP2- 020	L	1	80

Titolo:

Sviluppo codice FEM-LCORE per la simulazione del regime transitorio

PAGINA DI GUARDIA

Descrittori

Tipologia del documento: Rapporto Tecnico

Collocazione contrattuale: Accordo di programma ENEA-MSE su sicurezza nucleare e reattori di IV generazione

Argomenti trattati: Termoidraulica dei reattori nucleari
Termoidraulica del nocciolo
Generation IV reactors

Sommario

Si presenta lo sviluppo del codice di calcolo FEM-LCORE con approccio multiscala e moduli di tipo CFD e CFD per mezzi porosi, secondo geometrie tridimensionali e monodimensionali. Circuito primario di un reattore nucleare, plenum e nocciolo sono rappresentati mediante tre livelli di scala: rispettivamente 1-D per mezzi porosi, tipo CFD 3-D e 3-D per mezzi porosi. Interfacce fra moduli 3D-CFD e 3D-poroso e anche fra 3D-CFD e 1D-poroso risolvono le equazioni 3D e 1D attraverso un unico solutore non lineare accoppiato. Oggetto di studio, con modello multiscala, è il transitorio del reattore sia in convezione naturale che in condizioni nominali. Questo lavoro costituisce un elemento verso un accoppiamento di FEM-LCORE con codici di calcolo 1D più sofisticati, inerenti l'analisi di sistema e la sicurezza nucleare. FEM-LCORE studia l'evoluzione temporale del comportamento di un reattore in caso di danneggiamento o perdita di servizio delle pompe; quando il flusso di refrigerante è dovuto soltanto alla circolazione naturale. La nuova versione considera la solidificazione del refrigerante mediante un modulo che tratta questo aspetto cruciale nell'ambito delle simulazioni per reattori di IV Generazione refrigerati a piombo liquido. Inoltre il modello analizza casi in cui frazioni di piombo solido e liquido sono iniettate nel reattore a causa di eccesso di potenza rimossa agli scambiatori.

Note:

Rapporto emesso da Università di Bologna (UNIBO)

Autori:

D. Cerroni, S. Manservisi, E. Vincenzi (UNIBO)

Copia n. **In carico a:**

REV.	DESCRIZIONE	DATA		CONVALIDA	VISTO	APPROVAZIONE
2			NOME			
			FIRMA			
1			NOME			
			FIRMA			
0	EMISSIONE	23/09/2013	NOME	M. Tarantino	NA	M. Tarantino
			FIRMA			

CIRTEN
CONSORZIO INTERUNIVERSITARIO
PER LA RICERCA TECNOLOGICA NUCLEARE

DEVELOPING MULTISCALE TRANSIENT SIMULATIONS WITH FEM-LCORE CODE

AUTORI:
D. Cerroni, S. Manservisi and E. Vincenzi
DIN - University of Bologna,Via dei Colli 16, 40136 Bologna, Italy

Report RdS/2013/1355-UNIBO
DIN - ALMA MATER STUDIORUM - UNIVERSITÀ DI BOLOGNA
LABORATORIO DI MONTECUCCOLINO

Developing Multiscale Transient Simulations with FEM-LCORE code

D. Cerroni, S. Manservisi and E. Vincenzi
DIN - University of Bologna Via dei Colli 16, 40136 Bologna, Italy

September 1, 2013

Ricerca di Sistema Elettrico - PAR2013
Accordo di Programma Ministero dello Sviluppo Economico - ENEA
Linea progettuale LP2 punto C1f:
Sviluppo e validazione di codici per la termoidraulica LFR

e-mail: sandro.manservisi@unibo.it

Contents

ABSTRACT

In this report the development of the FEM-LCORE code is presented in its multiscale approach. Several three-dimensional and mono-dimensional CDF and CFD-porous modules are developed. The reactor primary circuit, the plenum and the core are modeled at three different scale levels with a 1D-porous, 3D-CFD and 3D-porous module, respectively. Appropriate interfaces between 3D-CFD/3D-porous and 3D-CFD/1D-porous are introduced in order to solve the three-dimensional and mono-dimensional equations through a unique non-linear coupled solver. The evolution of the reactor in natural convection or in working conditions is investigated with this multiscale modeling setting the first step in the direction of a coupling between FEM-LCORE and more sophisticated mono-dimensional nuclear safety system codes. With FEM-LCORE we study the time-evolution of the reactor for different thermal powers when the pumps are off and the flow is only provided by natural convection. The new version of the code is also improved by offering the opportunity to study coolant solidification. An extremely simplified model is introduced for studying the freezing phenomenon for lead cooled reactors. With this model we study some simple cases when, due to excessive cooling of the heat exchanger, a mixture of solid/liquid lead is injected in the reactor.

Introduction

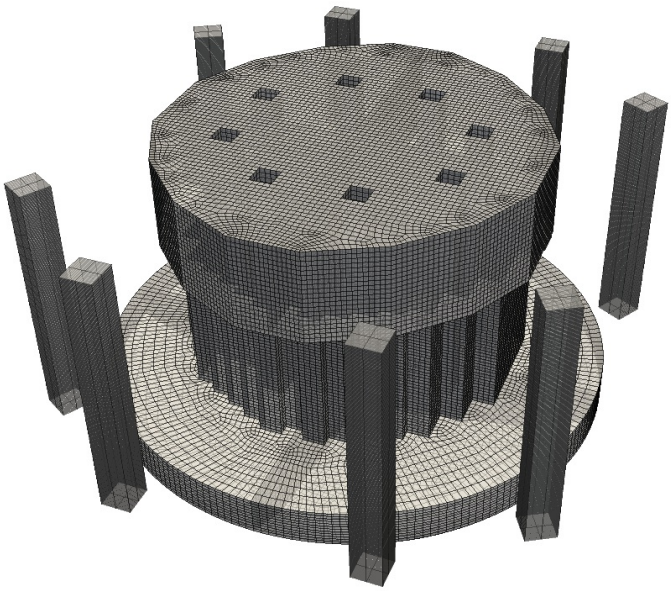

Figure 1: A computational three-dimensional reactor model for FEM-LCORE code

The understanding of the thermohydraulics of Generation IV reactors is the starting point to improve safety and to optimize the use of fuel resources. Since a detailed study, which takes into account the design of all the reactor channels inside all the assemblies, is not possible with the current available computational power, it is necessary to solve the problem with a multiphysics and multiscale approach. To study the transient behavior of the system one has to take into account all the parts that compose the primary loop of the system. The central of the reactor including the plenum and the core may be investigated with a three dimensional model at different scale levels. The plenum can be studied with standard CFD model while the core and the primary circuit may be modeled with a porous media approach. The rest of the primary circuit can be analyzed with a mono-dimensional system in

which different components, such as steam generator, pumps, etc., are considered.

FEM-LCORE is a 3D/1D finite element code, developed at the University of Bologna in collaboration with ENEA, for the simulation of the thermo-hydraulic behavior of the core and the plenum of liquid metal nuclear reactors. The FEM-LCORE code estimates three-dimensional average temperature, pressure and velocity fields, of a computing reactor model, as shown in Figure 1, by properly modeling the complexity of the sophisticated parts (core, steam generator, etc.) with a lead-cooled porous medium. The new version improves the modeling of the behavior of the reactor by coupling three-dimensional solutions with mono-dimensional ones allowing to analyze transient phenomena. This is the first step in the direction of coupling FEM-LCORE with a system code, like CATHARE, to simulate the entire primary loop inside the SALOME platform. At the moment the CATHARE-SALOME and FEM-LCORE-SALOME integration modules are still under development. Moreover the complete simulation of the primary loop allows the analysis of natural convection flows. The new version of the code improves also the modeling of liquid metal offering the opportunity to study freezing phenomena.

Chapter 1 is devoted to the multiscale approach. We briefly recall the set of equations adopted for the thermo-hydraulic reactor modeling and for the 3D-CFD, 3D-porous, 1D-CFD and 1D-porous modules. A brief description of the coupling method is provided.

In Chapter 2 there is a description of the reactor components that are considered in our simulations. We test the reactor at different power levels when the pumps are off and lead flow is only provided by natural convection. Results of the evolution of temperature, velocity and pressure fields in the reactor and in the primary loop are reported.

Chapter 3 starts with a brief description of the simple freezing model implemented in the code. In the rest of the chapter we present some test cases where a mixture of solid/liquid lead is injected in the reactor.

Chapter 1

Developing multiscale FEM-LCORE

1.1 Multiscale approach to LFR

A nuclear plant is a very complex system. The central part of a LFR consists of several components and their accurate simulation cannot be performed in three-dimensional space with the actual computational power. For this reason it seems reasonable a multiscale approach where different components are studied on different scales based on a well defined computing resource plan. As shown in Figure 1.1, one can see four representative different scales: DNS, CFD, porous and system scale.

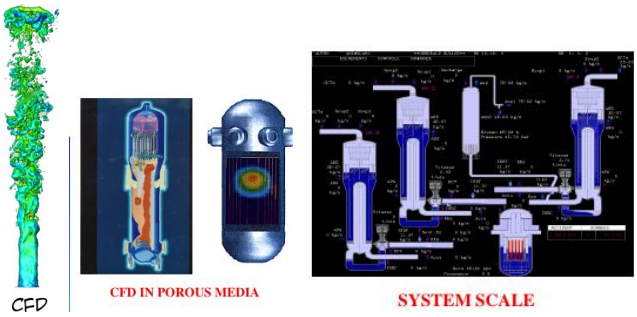

Figure 1.1: CFD (3D), porous (3D) and system scale (1D)

The scale where the Navier-Stokes can be solved to define completely the physics of the system is called DNS or Direct Numerical Simulation scale. The CFD scale is the scale where the usual Computational Fluid Dynamics codes can approximate satisfactory the system evolution. This includes turbulence models that usually cannot be simulated in the DNS scale. In the porous model scale the geometrical details are so numerous that a detailed simulation cannot be possible in the DNS scale. In this scale the introduction of a unique fictitious porous material with average properties must be considered. Finally in the system scale all the components are considered

through a mono-dimensional or zero-dimensional model in order to study the global behavior of several components against desired plant control.

FEM-LCORE code is an in-house code developed in collaboration between ENEA and the University of Bologna to simulate the thermohydraulics behavior of a LFR reactor. The code has been written with multiscale approach and it consists of 3D-CFD/3D-porous, 2D-CFD/2D-porous and 1D-CFD/1D-porous modules. The modules work independently and one or more modules may be substituted by well known codes. For example the 1D-porous module may be replaced with CATHARE code, which implements lead properties, since it can perform 1D transient computations of the primary loop. In order to do this we plan to integrate the FEM-LCORE code in the open-source SALOME platform where the CATHARE code is going to be implemented for purpose of integration with other proprietary CEA codes. At the moment the integration with the SALOME platform is in development. For details see [10]. FEM-LCORE has a graphical user interface (GUI) that integrates the code inside the SALOME platform. Once integrated in this platform, FEM-LCORE could use all the resources available inside the platform: meshing visualization, integration with other codes, etc. The SALOME platform is the reference platform chosen by some European nuclear thermohydraulics projects, such as CATHARE, SATURNE, aiming a partial or complete crossing code integration [29]. Once the integration among all the codes is terminated, SALOME platform will be able to simulate multiphysics and multiscale problems. SALOME platform could run sequentially different codes as a unique segregated solver. At the moment the integration of the SALOME platform with codes such as CATHARE is in developing phase through European projects. CATHARE and other codes are developed by CEA and are not open to the public. The SALOME platform, as FEM-LCORE code, is a open source code

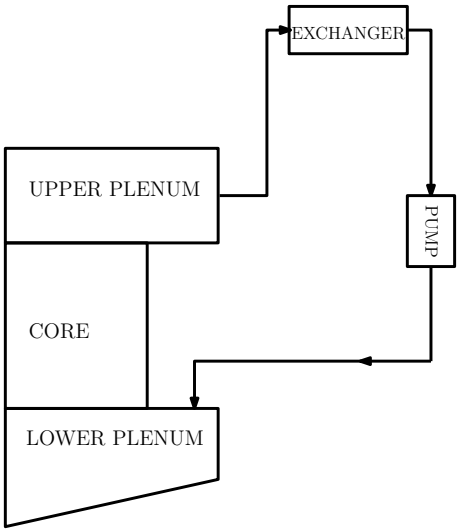

Figure 1.2: FEM-LCORE multiscale model

and uses only open source libraries. FEM-LCORE code is based on FEMuS code developed at the University of Bologna for more general purposes. FEM-LCORE has a parallel and multigrid solver based on PETSC libraries. The mesh for the 3D computations can be generated by GAMBIT and SALOME mesh generator. The geometrical multigrid mesh is generated by the LIBMESH libraries [31, 32]. The code is written in C++ object oriented language with parallel multigrid solver based on the PETSC libraries [26, 25, 28] the Graphical User Interface (GUI) in PY-QT. The GUI is fully compatible with SALOME in the framework of the QT libraries and based on SATURNE integration module. For more details see [11, 12].

In FEM-LCORE code a simple multiscale approach is adopted. As shown in Figure 1.2 we consider the LFR system basically divided into three regions: heat exchange loop (1D-porous), plenum (3D-CFD) and core (3D-porous) region. The 3D-CFD and 1D-CFD modules are models for one-fluid flows only. The 3D-porous and 1D-porous modules may contain fluid and structural material which stands still with respect to the fluid motion. The 3D-porous and 1D-porous modules may define complex systems such a series of fuel assembly or tubes of an heat exchanger.

1.2 3D-CFD scale

1.2.1 General model description

FEM-LCORE multiscale is based on the conservative equations which are integrated at the different scales. On 3D-CFD scale the three-dimensional conservative incompressible equations in velocity, pressure and enthalpy (or temperature) field $(\mathbf{v}, p, h(T))$ over a domain Ω with boundary Γ are the following

$$\nabla \cdot (\rho\, \mathbf{v}) = 0\,, \tag{1.1}$$

$$\frac{\partial \rho\, \mathbf{v}}{\partial t} + \nabla \cdot (\rho \mathbf{v}\mathbf{v}) = -\nabla p + \nabla \cdot \bar{\tau} + \rho \mathbf{g}\,, \tag{1.2}$$

$$\frac{\partial \rho\, h}{\partial t} + \nabla \cdot (\rho \mathbf{v}\, h) = \Phi + \nabla \cdot (\frac{k_f}{C_p} \nabla h) + \dot{Q}\,, \tag{1.3}$$

where ρ is the density, $\mathbf{g}$ the gravity acceleration vector, C_p is the pressure specific heat, k_f the effective heat conductivity, $\dot{Q}$ the volume heat source and Φ the dissipative heat term. The enthalpy h is defined by

$$h = C_p\, T\,, \tag{1.4}$$

with C_p constant in the liquid region. The use of h or T is completely indifferent. We use the temperature T as a main variable but we refers to enthalpy when the liquid and the solid phase are present at the same time. We assume pressure solution in the space $P(\Omega)$, velocity in $\mathbf{V}(\Omega)$ and temperature in $H(\Omega)$. For details see [8, 9, 10].

The viscous stress tensor $\bar{\tau}$ is defined by

$$\bar{\tau} = 2\mu_f \bar{D}(\mathbf{u}), \quad D_{ij}(\mathbf{u}) = \frac{1}{2}(\frac{\partial u_i}{\partial x_j} + \frac{\partial u_j}{\partial x_i}),$$

where $\mu_f = \mu_l + \mu_t$ is the effective viscosity. The turbulent viscosity μ_t and the effective heat conductivity k_f are defined by a system of equations modeling the turbulent model. For details see [9, 10]. The incompressibility constraint (1.1) is assumed to be valid even if the density is supposed to be dependent on temperature.

These equations should be averaged in space depending on the scale. For this purpose we introduce their variational form. The variational form of the incompressible mass conservation equation can be obtained by multiplying by $\psi \in P(\Omega)$ the (1.1) as

$$\int_\Omega \psi \nabla \cdot \mathbf{v}\, d\mathbf{x} = 0 \quad \forall \psi \in P(\Omega). \tag{1.5}$$

In a similar way the momentum and energy equation in variational form can be obtained by multiplying the (1.2) and (1.3) by $\phi \in \mathbf{V}(\Omega)$ and $\varphi \in H(\Omega)$, respectively. For the momentum equation we have

$$\begin{aligned}\int_\Omega \frac{\partial \rho \mathbf{v}}{\partial t} \cdot \phi\, d\mathbf{x} + \int_\Omega (\nabla \cdot \rho \mathbf{v}\mathbf{v}) \cdot \phi\, d\mathbf{x} = -\int_\Gamma (p\vec{n} - \bar{\tau} \cdot \vec{n}) \cdot \phi\, d\mathbf{s} + \\ \int_\Omega p \nabla \cdot \phi\, d\mathbf{x} - \int_\Omega \bar{\tau} : \overline{\nabla \phi}\, d\mathbf{x} + \int_\Omega \rho \mathbf{g} \cdot \phi\, d\mathbf{x} \qquad \forall \phi \in \mathbf{V}(\mathbf{\Omega}).\end{aligned} \tag{1.6}$$

For the energy equation we have

$$\begin{aligned}\int_\Omega \frac{\partial \rho C_p T}{\partial t} \varphi\, d\mathbf{x} + \int_\Omega \nabla \cdot (\rho \mathbf{v} C_p T) \varphi\, d\mathbf{x} = \int_\Omega \Phi \varphi\, d\mathbf{x} \\ - \int_\Omega k_f \nabla T \cdot \nabla \varphi\, d\mathbf{x} + \int_\Omega \dot{Q} \varphi\, d\mathbf{x} + \int_\Gamma (k_f \nabla T \cdot \vec{n}) \varphi\, d\mathbf{s} \quad \forall \varphi \in \mathbf{H}(\Omega)\end{aligned} \tag{1.7}$$

The surface integrals are defined by the boundary conditions. The test functions ψ, ϕ, φ are the weight to average the equation over the scale.

If we consider a domain discretization and the corresponding subspaces of $P(\Omega)$, $\mathbf{V}(\Omega)$ and $H(\Omega)$ parametrized by the element length h, the system (1.5-1.7) can be identified with its numerical approximation. We remark that setting $P(\Omega) = P_h \subset L^2_0(\Omega)$, $\mathbf{V}(\Omega) = \mathbf{X}_h \subset \mathbf{H}^1(\Omega)$ and $H(\Omega) = X_h \subset H^1(\Omega)$ gives finite dimensional solution with the Finite Element Method (FEM). If one sets $P(\Omega) = P_h \subset L^2_0(\Omega)$, $\mathbf{V}(\Omega) = \mathbf{X}_h \subset \mathbf{L}^2(\Omega)$ and $H(\Omega) = X_h \subset L^2(\Omega)$ then one has a finite dimensional solution with the Finite Volume Method (FVM). As $h \to 0$ we have the continuous solution. For details see [7, 8, 9, 10]

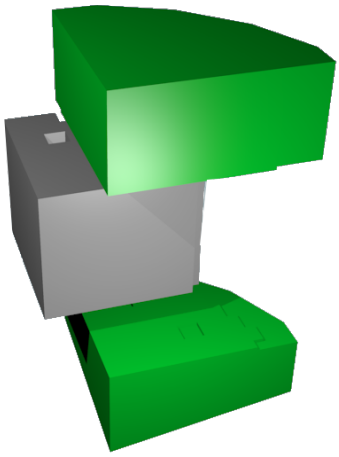

Figure 1.3: Schematic of the plenum volumes (in green)

1.2.2 Plenum model (3D-CFD module)

In the reactor there are two plena: the upper plenum and the lower plenum located below and above the core, respectively. The module that describes a Plenum module is basically a standard 3D-CFD module. In these regions below and above the core, the coolant flows in a quite open three-dimensional domain and the coolant state, defined by velocity $\mathbf{v}$, pressure p and temperature T, can be determined by

- Mass conservation equation, defined in (1.1)
- Momentum conservation equation, defined in (1.2)
- Energy equation, defined in (1.3)

In this region the density, the viscosity, the thermal conductivity and specific thermal capacity can be a function of temperature. For example the density can be a function defined as $\rho = \rho(T) = a + bT$. The equations (1.1-1.3) are stabilized with a standard up-wind for FEM.

Since the motion is turbulent the code solves the three-dimensional conservation equations coupled with turbulence models. In particular the module can use simple turbulence models such as

- $\kappa - \epsilon$ turbulent model,
- $\kappa - \omega$ turbulent model,
- Large Eddy Simulation (LES) turbulent model.

The turbulence models are implemented as presented in [21, 22, 23, 24] The turbulence coefficients can be defined in the MGclass_conf.h file.

1.3 1D-CFD scale (one-fluid system scale)

1.3.1 Model description

The 1D-CFD module used in FEM-LCORE is obtained by integrating (1.5-1.7) with mono-dimensional weight functions. Briefly one can set $\psi = \psi(s)$, $\phi = \phi(s)$ and $\varphi = \varphi(s)$ implying that the test functions are only a function of the mono-dimensional coordinate s. This module is properly used for mono-dimensional flows such as channels with single fluid.

1D-CFD mass equation. Let A be a surface perpendicular to the center-line. Over the surface A we define average density and average velocity as

$$\bar{\rho} = \frac{\int_A \rho \, dA}{A} \qquad \bar{v} = \frac{\int_A \rho \, v \, dA}{\bar{\rho} A} \, . \tag{1.8}$$

With this definition we write

$$\int_0^L \psi(s) \, \frac{\partial}{\partial s} \, (\bar{\rho} \, \bar{v} \, A) \, ds = \int_0^L \psi(s) \, S_s \, ds \quad \forall \psi \in P(0, L) \, , \tag{1.9}$$

where S_s is the mass source from surface integral. Usually $S_s \approx 0$.

1D-CFD momentum equation. In a similar way for the average quantities ($\bar{\rho}$, $\bar{v}$, $\bar{p}$) and $\phi \approx \phi(s)$ the momentum equation becomes

$$\begin{aligned} \int_0^L \bar{\rho} \, A \, (\frac{\partial}{\partial t} \, \bar{v}) \, \phi(s) \, ds + \int_0^L \bar{\rho} \bar{v} \, A \, (\frac{\partial}{\partial s} \, \bar{v}) \, \phi \, ds = \int_0^L \bar{p} \, A \, \frac{\partial}{\partial s} \, \phi \, ds \\ \int_0^L A \bar{\rho} \mathbf{g} \cdot \widehat{i}_s \, \phi \, ds + \int_0^L \phi(s) \, (M_s + M_v) \, ds \qquad \forall \phi \in V(0, L) \, , \end{aligned} \tag{1.10}$$

where M_s is from surface integral and M_v from volume contributions. Usually $M_s \approx -k \, \frac{\rho}{2} \, \bar{u}|\bar{u}|$ (pressure loss). The volume contribution M_v consists of several terms. Is is easy to see that $M_v = M_{v,\tau}(\bar{\tau}) + M_{v,vv}(\bar{\mathbf{v}}\bar{\mathbf{v}} - \bar{v}\bar{v})$ with obvious definition of the terms $M_{v,\tau}$ and $M_{v,vv}$. For details see [7, 8].

1D-CFD energy equation. For the Energy equation the average quantities involved are ($\bar{\rho}$, $\bar{v}$, $\bar{p}$, $\bar{T}$) and the equation becomes

$$\begin{aligned} \int_0^L \frac{\partial \, A \, \bar{\rho} \, C_p \, \bar{T}}{\partial t} \, \varphi(s) \, ds + \int_0^L (\frac{\partial}{\partial s} \, (A \, \bar{\rho} \, \bar{v} C_p \, \bar{T}) \, \varphi \, ds = \\ - \int_0^L \dot{Q}_s \varphi \, d\mathbf{x} + \int_0^L \dot{Q}_v \varphi \, ds \quad \forall \varphi \in \mathbf{H}(\Omega) \, . \end{aligned} \tag{1.11}$$

We have a contribution from the boundary and a contribution from the volume. From surface integrals we define Q_s (heat exchange through surfaces). From volume

integral (volume interaction) we define

$$Q_v = Q_{v,q}(\bar{\tau}) + Q_{v,vv}(\bar{\mathbf{v}\mathbf{T}} - \bar{v}\bar{T}) + Q_{v,\Phi}(\Phi) \tag{1.12}$$

with $Q_{v,q}$ internal heat conduction and $Q_{v,vv}$ turbulent term. For details see [7, 8].

1D-CFD scale model. In standard form (non variational form) the 1D-CFD scale model, defined by (1.9-1.11), can be written as follows

$$\frac{\partial}{\partial s}\big(\,\bar{\rho}\,\bar{v}\,A\big) = 0\,. \tag{1.13}$$

$$\frac{\partial}{\partial t}\,A\bar{\rho}\bar{v} + \bar{\rho}\,A\,\bar{v}\frac{\partial}{\partial s}\big(\,\bar{v}\,\big) + \,A\,\frac{\partial}{\partial s}\,P = -\,k\,\frac{\bar{\rho}}{2}\,\bar{v}|\bar{v}| + \bar{\rho}\,A\,g_s + M_v\,. \tag{1.14}$$

$$\frac{\partial}{\partial t}A\,\bar{\rho}\,C_p\,\bar{T} + \frac{\partial}{\partial s}\,A\,\bar{\rho}\,\bar{v}\,C_p\,\bar{T} = \rho\,A\,\bar{v}\,g_s + \bar{Q}_s + \bar{Q}_v\,. \tag{1.15}$$

The first equation states that the mass flux $\dot{m} = \bar{\rho}\,\bar{v}\,A$ is constant in space. The second equation is the transient Bernoulli equation and with no sources ($M_s = M_v = 0$) it states that $P + \rho v^2/2 + \rho g_s$ is constant in space.

1.4 3D-porous scale (components)

1.4.1 Model description

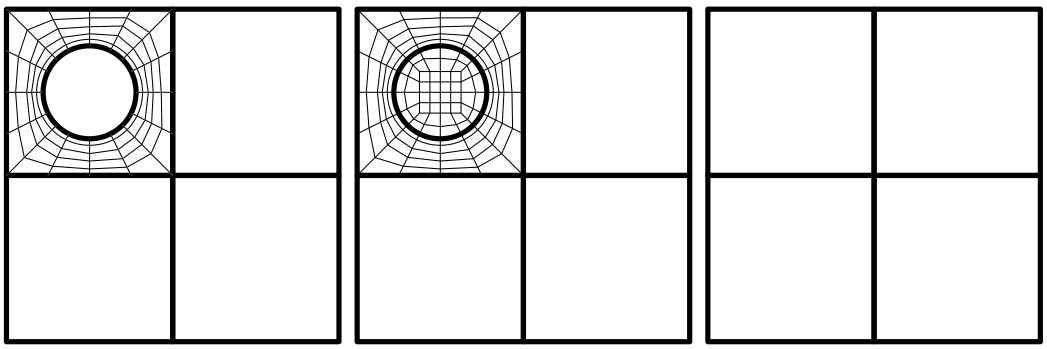

Figure 1.4: Two level solution scheme: geometrical fine (left), fine (middle) and coarse (right) level

In many components the simulation of internal flows is very complex and simplifying assumptions should be in order. For example we can consider the core case where there are hundreds of assemblies and each assembly has hundreds of fuel rods. The complexity of this geometry asks for domain homogenization. As shown

in Figure 1.4 on the left one can see the geometrical fine grid of the fluid domain where the rod fuel is defined by the circle in the middle of the square region. In the center of Figure 1.4 the mesh is extended to the solid region. On the right only the coarse mesh is shown. The multiscale procedure is simple: the original solution on the fluid region can be extended to the solid zone and then projected on the coarse grid considering a new mixture material.

3D-porous mass equation. In order to illustrate this multiscale procedure one can consider the mass conservation equation in strong (left) and variational (right) form over the domain Ω

$$\nabla \cdot \rho \mathbf{v} = 0 \qquad \int_{\Omega} \nabla \cdot \rho \, \mathbf{v} \, \psi \, d\mathbf{x} = 0 \, . \tag{1.16}$$

In the first step the domain is extended $\Omega \to \widehat{\Omega}$ and the (1.16) written as

$$\int_{\widehat{\Omega}} \nabla \cdot \rho \mathbf{v} \, \psi \, d\mathbf{x} = 0 \, , \tag{1.17}$$

with density and velocity field extended on $\widehat{\Omega}$. Now we project the equation on the fine grid over test base function $\psi_h(k)$

$$\int_{\widehat{\Omega}_h} \nabla \cdot \rho \mathbf{v}_h \, \psi_h(k) \, d\mathbf{x} = 0$$

and consider the solution $(\widehat{\mathbf{v}}, \widehat{p}, \widehat{T})$ on the coarse grid with test functions $\widehat{\psi}_h(j)$.

If the fine test base function $\psi_h(k)$ is a complete set in the coarse grid then we have

$$\widehat{\psi}_h(j) = \sum_k C_{kj} \, \psi_h(k) \qquad \widehat{\mathbf{v}}_h = \sum_j \mathbf{v}_j \sum_k C_{kj} \, \psi_h(k) \, .$$

The sum over the equation involving $\widehat{\mathbf{v}}_h$ on a coarse level becomes

$$\sum_k C_{kj} \int_{\widehat{\Omega}_h} \nabla \cdot \rho \mathbf{v}_h \, \psi_h(k) \, d\mathbf{x} = \int_{\widehat{\Omega}_h} \nabla \cdot \rho \mathbf{v}_h \, \widehat{\psi}_h(j) \, d\mathbf{x} = 0$$

or

$$\int_{\widehat{\Omega}_h} \nabla \cdot \rho (\mathbf{v}_h + \widehat{\mathbf{v}}_h - \widehat{\mathbf{v}}_h) \, \widehat{\psi}_h(j) \, d\mathbf{x} = 0 \, .$$

Therefore the incompressibility constraint can be written as

$$\int_{\widehat{\Omega}_h} \nabla \cdot \rho \, \widehat{\mathbf{v}}_h \, \widehat{\psi}_h(j) \; d\mathbf{x} = \int_{\widehat{\Omega}_h} P^c_{ef}(\widehat{\mathbf{v}}_h, \, \mathbf{v}_h) \, \widehat{\psi}_h(j) \, d\mathbf{x} \quad \forall \widehat{\psi}_h(j) \, ,$$

with the mass fine-coarse transfer operator P^c_{ef} defined by

$$P^c_{ef}(\widehat{\mathbf{v}}_h, \mathbf{v}_h) = \nabla \cdot \rho(\widehat{\mathbf{v}}_h - \mathbf{v})\,.$$

Usually one assumes

$$R^c_{ef} = \int_{\widehat{\Omega}_h} P^c_{ef}(\widehat{\mathbf{v}}_h,\, \mathbf{v}_h)\, \widehat{\psi}_h(j)\, d\mathbf{x} \approx \int_{\widehat{\Omega}_h} \nabla \cdot\, \zeta\, \rho \widehat{\mathbf{v}}_h\, \widehat{\psi}_h(j)\, d\mathbf{x} \quad \forall \widehat{\psi}_h(j)\,,$$

where ζ is the fraction of the structural material in the volume. In final form we can write

$$\int_{\widehat{\Omega}_h} \nabla \cdot (1-\zeta)\rho\, \widehat{\mathbf{v}}_h\, \widehat{\psi}_h(j)\; d\mathbf{x} = 0\,. \tag{1.18}$$

The (1.18) implies that the velocity in the porous media is $(1-\zeta)\,\widehat{\mathbf{v}}_h$ while the real velocity in the fluid is $\widehat{\mathbf{v}}_h$. The velocity $(1-\zeta)\,\widehat{\mathbf{v}}_h$ is called reduced velocity. The liquid mass flux is $\rho\,\widehat{\mathbf{v}}_h \cdot \mathbf{n} A_f$ with A_f the fluid area and $\mathbf{n}$ the unit normal. If we add the area A_m of the structural material then the liquid mass flux through the porous media area $A = A_f + A_m$ is $\rho\,\widehat{\mathbf{v}}_h \cdot \mathbf{n} A$ which is $(1-\zeta)$ times greater than the real one.

3D-porous momentum equation. In a similar way we can write the momentum equation as [7, 8]

$$\begin{aligned}
\int_\Omega \frac{\partial\, \rho\, \widehat{\mathbf{v}}_h}{\partial t} \cdot \widehat{\phi}_{hj}\, d\mathbf{x} + \int_\Omega (\nabla \cdot \rho\, \widehat{\mathbf{v}}_h \widehat{\mathbf{v}}_h) \cdot \widehat{\phi}_{hj}\, d\mathbf{x} - \\
\int_\Omega \widehat{p}_h\, \nabla \cdot \widehat{\phi}_h(k)\, d\mathbf{x} + \int_\Omega \bar{\bar{\tau}}_h : \nabla \widehat{\phi}_{hj}\, d\mathbf{x} - \int_\Omega \rho \mathbf{g} \cdot \widehat{\phi}_{hj}\, d\mathbf{x} = \\
\int_\Omega R^m_{cf}(p_h, \mathbf{v}_h, \widehat{p}_h, \widehat{\mathbf{v}}_h) \cdot \widehat{\phi}_{hj}\, d\mathbf{x}\,,
\end{aligned}$$

where the fine-coarse transfer operator $R^m_{cf}(p_h, \mathbf{v}_h, \widehat{p}_h, \widehat{\mathbf{v}}_h)$ is defined by

$$R^m_{cf}(p_h, \mathbf{v}_h, \widehat{p}_h, \widehat{\mathbf{v}}_h) = P^m_{cf}(\widehat{p}_h - p_h, \widehat{\mathbf{v}}_h - \mathbf{v}_h) + T^m_{cf}(\mathbf{v}_h, \widehat{\mathbf{v}}_h) + K^m_{cf}(\mathbf{v}_h)$$

where

$$\int_\Omega P^m_{cf}(\widehat{p}_h - p_h, \widehat{\mathbf{v}}_h - \mathbf{v}_h) \cdot \widehat{\phi}_{hj}\, d\mathbf{x} \tag{1.19}$$

is the volume fine-coarse term

$$\int_\Omega T^m_{cf}(\mathbf{v}_h, \widehat{\mathbf{v}}_h) \cdot \widehat{\phi}_{hj}\, d\mathbf{x} \tag{1.20}$$

is the nonlinear (turbulent) term and

$$\int_\Omega K^m_{cf}(\mathbf{v}_h) \cdot \widehat{\phi}_{hj}\, d\mathbf{x} = \int_\Gamma (-p_h\, \vec{n} + \tau_h \cdot \vec{n}) \cdot \widehat{\phi}_{hj}\, d\mathbf{s} \tag{1.21}$$

the pressure term. For details see [7, 8, 9, 10].

3D-porous energy equation. For the energy equation, by applying the same procedure, we have [7, 8]

$$\int_\Omega \frac{\partial\, \rho\, C_p\, \widehat{T}_h}{\partial t}\, \widehat{\varphi}_{hj}\, d\mathbf{x} + \int_\Omega \widehat{\varphi}_{hj}\, \nabla\cdot \rho\, C_p \widehat{\mathbf{v}}_h\, \widehat{T}_h\, d\mathbf{x}$$
$$\int_\Omega k\, \nabla \widehat{T}_h \cdot \nabla \widehat{\varphi}_{hj}\, d\mathbf{x} - \int_\Omega Q_h\, \widehat{\varphi}_{hj}\, d\mathbf{x} = \int_\Omega R^e_{cf}(T_h)\, \widehat{\varphi}_{hj}\, d\mathbf{x}$$

where the energy source from the fine scale is R^e_{cf}, i.e.,

$$R^e_{cf}(T_h) = S^e_{cf}(T_h) + P^e_{cf}(\widehat{T}_h - T_h, \widehat{\mathbf{v}}_h - \mathbf{v}_h) + T^e_{cf}(\widehat{\mathbf{v}}_h, \mathbf{v}_h)$$
$$\int_\Omega S^e_{cf}(T_h)\, \widehat{\varphi}_{hj}\, d\mathbf{x} = \int_\Gamma k\, (\nabla T_h \cdot \vec{n})\, \widehat{\varphi}_{hj}\, d\mathbf{x} \quad \text{fuel heat source}$$
$$\int_\Omega P^e_{cf}(\widehat{T}_h - T_h, \widehat{\mathbf{v}}_h - \mathbf{v}_h)\, \widehat{\varphi}_{hj}\, d\mathbf{x} = \text{volume term}$$
$$\int_\Omega T^e_{cf}(\widehat{\mathbf{v}}_h, \mathbf{v}_h)\, \varphi_{hj}\, d\mathbf{x} = \text{nonlinear (turbulence) term}\ .$$

For details see [7, 8].

3D-porous model. In order to complete the 3D-porous model one must model all these terms. Usually the turbulence operators T^m_{cf}, T^e_{cf} are included in the turbulence model as

$$T^e_{cf}(\widehat{T}_h, T_h, \widehat{\mathbf{v}}_h, \mathbf{v}_h) = \nabla\cdot(\frac{\mu_{tf}}{Pr_t}\nabla\widehat{T}_h)\,,$$
$$T^m_{cf}(\widehat{\mathbf{v}}_h, \mathbf{v}_h) = \nabla\cdot\mu_{t1}(\nabla\widehat{\mathbf{v}}_h + \nabla\widehat{\mathbf{v}}_h^T)\,,$$

with μ_{t1} the turbulent viscosity term that comes from the fine grid. The P^m_{cf} and P^e_{cf} are modeled as

$$P^e_{cf}(T_h - \widehat{T}_h) = \tag{1.22}$$
$$\Big(\frac{\partial\zeta\,\rho\, C_p\, \widehat{T}_h}{\partial t} + \nabla\cdot(\,\zeta\rho\, C_p \widehat{\mathbf{v}}_h\, \widehat{T}_h) - \zeta\Phi_h - \nabla\cdot(\,\zeta\, k^{eff}\nabla\widehat{T}_h) - \zeta\rho\mathbf{g}\Big)\,,$$

and

$$P^m_{cf}(\widehat{p}_h - p_h, \widehat{\mathbf{v}}_h - \mathbf{v}_h) = \tag{1.23}$$
$$\Big(\frac{\partial\,\zeta\,\rho\,\widehat{\mathbf{v}}_h}{\partial t} + (\nabla\cdot\,\zeta\,\rho\,\widehat{\mathbf{v}}_h\widehat{\mathbf{v}}_h) + \nabla\cdot\,\zeta\,\widehat{p}_h - \nabla\cdot\,\zeta\widehat{\tau}_h - \nabla\cdot\zeta\,\widehat{\tau}^{eff}{}_h\Big)\,,$$

where ζ is the fraction of structural material in the volume. k^{eff} and $\widehat{\tau}^{eff}$ must be defined from direct simulation or experiments. The heat source from the fine scale

$S^e_{cf}(p_h)$ (from fuel pin) may be modeled as

$$S^e_{cf}(p_h) = W = W_0 \cos(\pi \frac{z - .5\,(H_{out} + H_{in})}{H_{out} - H_{in}})\,, \tag{1.24}$$

where $H_{in}$and H_{out} are the heights where the heat generation starts and ends. The nuclear heat plane distribution W_0 comes from neutronics computations.

This leads to the 3D-porous system of equations strong form to take the following form

$$\nabla \cdot r\,\rho\,\widehat{\mathbf{v}} = 0\,, \tag{1.25}$$

$$\frac{\partial r\,\rho\,\widehat{\mathbf{v}}}{\partial t} + (\nabla \cdot r\,\rho\,\widehat{\mathbf{v}}\widehat{\mathbf{v}}) = -\nabla(r\,\widehat{p} + \widehat{p}_l) + \nabla \cdot \left(r\,(\widehat{\tau} + \widehat{\tau}^{\tau} + \bar{\widehat{\tau}}^{eff})\right) + r\rho\mathbf{g}\,, \tag{1.26}$$

$$\frac{\partial\, r\,\rho\, C_p\,\widehat{T}}{\partial t} + \nabla \cdot (r\,\rho C_p \widehat{\mathbf{v}}\,\widehat{T}) = \nabla \cdot \left(r\,(k + k^{eff} + \frac{\mu_t}{Pr_t})\,\nabla\widehat{T}\right) + r\,Q + W\,, \tag{1.27}$$

where $r = 1 - \zeta$. We remark that the main terms coming from the fine grid are the surface terms $W(\mathbf{x})$ and $\widehat{p}_l$. We note that the system (1.25-1.27) resembles the system of conservative equations for two-phase flow.

1.4.2 CORE model (3D-porous module)

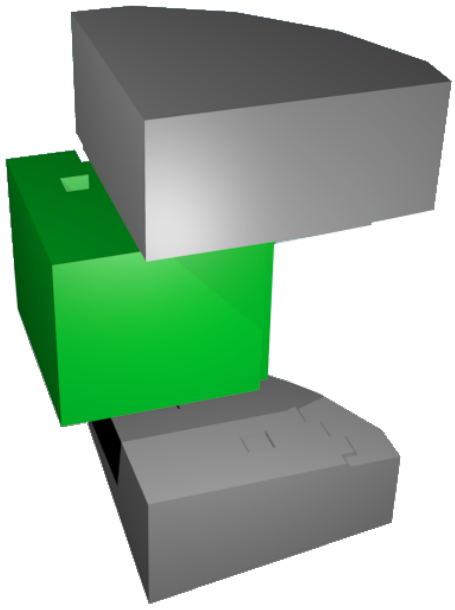

Figure 1.5: Core model. Schematic of the core volume (in green)

Equation model. In the core region the geometry is so complex and detailed that a porous model approximation is necessary since a direct simulation of the velocity, pressure and temperature distributions is not possible. For the core model

we use the 3D-porous module presented in the previous section. The 3D-porous module consists of the following equations:

- mass conservation equation defined in (1.25);
- momentum conservation equation defined in (1.26);
- energy equation defined in (1.27).

The turbulence model to be used in this porous medium is an open question and at the moment we have used the LES turbulent model. As shown in Figure 1.5 the 3D-porous module is connected with the 3D-CFD modules of the lower plenum and upper plenum. At these interfaces the fluid must flow from one module to the other and conserve the flow momentum. The 3D-CFD module in the plenum is different from the 3D-porous module since in the porous medium consists of fluid and solid material. This issue is going to be discussed in the interface model section.

The sources for the momentum and energy equations can be set in the MG-class_conf.h but the reactor core data has a special object class MGReactor which consists of the files MGReactor.C and MGReactor.h. All needed data for fuel and pressure loss distribution must be set there.

Fuel distribution. The space heat power distribution is defined in two steps. First one must define the average value and then the fuel pick factors. The average value heat source $\dot{q}_v$ should be set in the parameter.h file independently of a space-dependent configuration. In order to obtain the assembly averaged specific $\dot{q}_v$ and

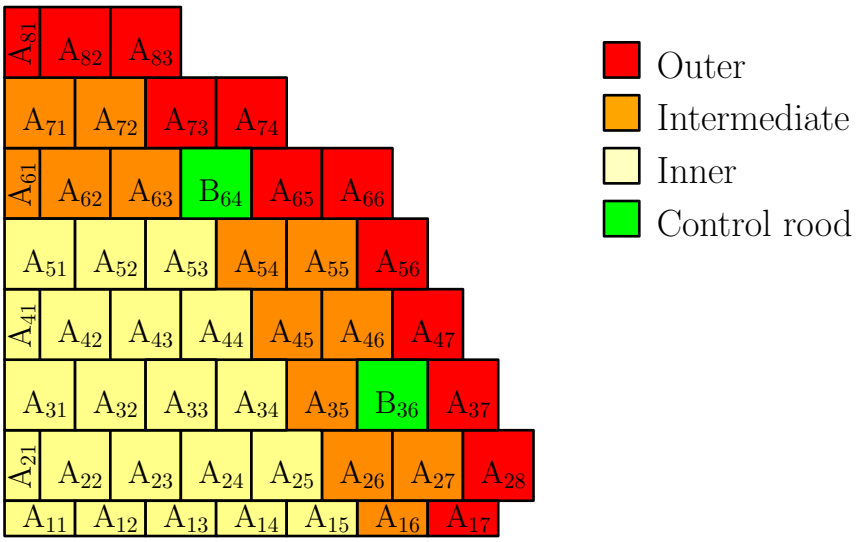

Figure 1.6: Core model. Core power distribution

linear $\dot{q}_l$ heat power, the total core power is to be divided over $N_a - 8$. We obtain

$$\dot{q}_l = \frac{\dot{Q}}{(N_a - 8) * L_{core}}$$

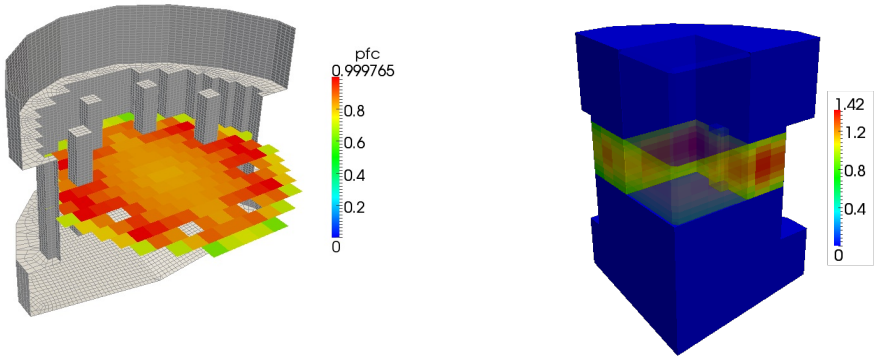

Figure 1.7: Core model. Computational vertical and horizontal core power distributions set in the MGReactor class

where A_{core} is

$$(N_a - 8) * A_{assembly}$$

$$\dot{q}_v = \frac{\dot{Q}}{(N_a - 8) * L_{core} * A_{assembly}},$$

where $\dot{Q}$ is the total heat thermal power, L_{core} the active core length. Then the space configuration of the heat source is taken into account by using peak factors. The computational heat power distribution is set in the `ReactData` class in the `SRC/ReactData.h` and `SRC/ReactData.C` files. In order to load the desired power distribution, one must set the following global configuration parameters in the header file: the number of elements in the vertical heated core section (NZC), half fuel assembly length (HR), heated core inlet height(HIN) and heated core outlet height (HOUT). A typical power distribution is shown in Figure 1.6. over the horizontal quarter section of the core. Each fuel assembly consists of a $n_p \times n_p$ pin lattice. The overall number of assembly positions in the core is N_a. Eight of these positions are dedicated to house special control rods and therefore the global number of fuel assemblies is N_{a-8}. For details one can see [15, 18, 1]. The transverse core area is approximately circular but not axial symmetric. Therefore, in order to predict accurately the behavior of the reactor, a three-dimensional simulation should be performed.

The model sets the fuel assemblies in three radial zones: N_{a1} fuel assemblies in the inner zone, N_{a2} fuel assemblies in the intermediate zone and the remaining N_{a3} fuel assemblies in the outer one. We label the assemblies as in Figure 1.6. The first row is labeled $A1$-i for $i = 1, \ldots, 8$, the second row $A2$-i for $i = 1, \ldots, 7$ and so on. We remark that the fuel assembly configuration is not based on a Cartesian grid but rather on a staggered grid. The power distribution factors, i.e. the power of each single fuel assembly over the average fuel assembly power, are mapped based on their row-column location.

In order to obtain the horizontal power distribution of Figure 1.7 we must be reported the pick factors in the double-indexed array `mat_pf` in the `ReactData` class, in which every assembly in the quarter of reactor is denoted by two indexes, both ranging from 0 to 7. The fuel area is divided into different zones, classified as inner core (I), outer core (O), control zone with no fuel (C) and reflector area (D). These are written in the `mat_zone` matrix as

$$\begin{array}{c} A1 \\ A2 \\ A3 \\ A4 \\ A5 \\ A6 \\ A7 \\ A8 \end{array} \begin{bmatrix} I & I & I & I & I & I & O & D \\ I & I & I & I & I & I & O & O \\ I & I & I & I & C & I & O & D \\ I & I & I & I & I & I & O & D \\ I & I & I & I & I & O & D & D \\ I & I & C & I & I & O & D & D \\ I & O & O & O & D & D & D & D \\ O & O & O & D & D & D & D & D \end{bmatrix} \\ \begin{array}{cccccccc} 1 & 2 & 3 & 4 & 5 & 6 & 7 & 8 \end{array}$$

with the corresponding horizontal power factor reported in the `mat_pf` matrix

$$\begin{array}{c} A1 \\ A2 \\ A3 \\ A4 \\ A5 \\ A6 \\ A7 \\ A8 \end{array} \begin{bmatrix} fp_{A11} & fp_{A12} & fp_{A13} & fp_{A14} & fp_{A15} & fp_{A16} & fp_{A17} & 0 \\ fp_{A21} & fp_{A22} & fp_{A23} & fp_{A24} & fp_{A25} & fp_{A26} & fp_{A27} & fp_{A28} \\ fp_{A31} & fp_{A32} & fp_{A33} & fp_{A34} & R & fp_{A36} & fp_{A37} & 0 \\ fp_{A41} & fp_{A42} & fp_{A43} & fp_{A44} & fp_{A45} & fp_{A46} & fp_{A47} & 0 \\ fp_{A51} & fp_{A52} & fp_{A53} & fp_{A54} & fp_{A55} & fp_{A56} & 0 & 0 \\ fp_{A61} & fp_{A62} & R & fp_{A64} & fp_{A65} & fp_{A66} & 0 & 0 \\ fp_{A71} & fp_{A72} & fp_{A73} & fp_{A74} & 0 & 0 & 0 & 0 \\ fp_{A81} & fp_{A82} & fp_{A83} & 0 & 0 & 0 & 0 & 0 \end{bmatrix} \\ \begin{array}{cccccccc} 1 & 2 & 3 & 4 & 5 & 6 & 7 & 8 \end{array} .$$

We remark that in the control area the pick factor is set to zero.

The vertical power factor can be assumed to have any distribution $g(z)$. This discrete profile is written in the `axpf` array as

$$\begin{bmatrix} Z_1 & g_I(Z_1) & g_O(Z_1) \\ Z_2 & g_I(Z_2) & g_O(Z_2) \\ Z_3 & g_I(Z_3) & g_O(Z_3) \\ Z_4 & g_I(Z_4) & g_O(Z_4) \\ Z_5 & g_I(Z_5) & g_O(Z_5) \\ Z_6 & g_I(Z_6) & g_O(Z_6) \end{bmatrix} \\ \begin{array}{ccc} height & I & O \end{array} , \tag{1.28}$$

where Z_i are the discrete vertical coordinates and $g_I(z)$ and $g_O(z)$ are the values in the INNER and OUTER zones.

Fuel rod temperature distribution. The simulation of the core introduced in the previous section takes into account average quantities over the assemblies and computes average coolant temperatures. When the coolant average temperatures are known then temperature profiles inside the fuel rod and the cladding can be computed by using standard assumptions and standard heat transfer correlations [5]. We remark that in the liquid metal case and in three-dimensional configura-

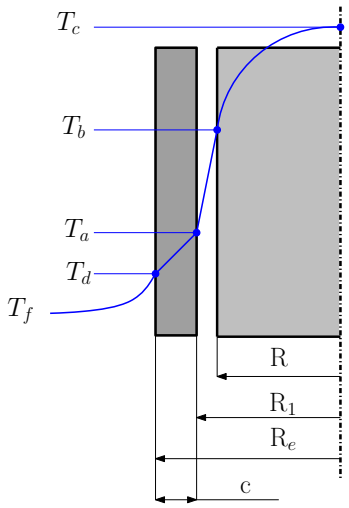

Figure 1.8: Temperature distribution in an assembly channel

tions the heat exchange coefficient may not be constant along the vertical coordinate and standard heat exchange models cannot be appropriate. The core computations previously proposed are able to define only average assembly temperatures. For temperatures inside the fuel rod we can use the average assembly coolant temperature T_f and standard analytical formulas. Let T_c be the temperature on the fuel rod axis and T_d the cladding temperature. We have

$$T_c = T_f + \Delta T_1 + \Delta T_2 + \Delta T_3 + \Delta T_4 = \\ T_f + (T_c - T_b) + (T_b - T_a) + (T_a - T_d) + (T_d - T_f)\,. \tag{1.29}$$

One may compute the temperature jump ΔT_1, ΔT_2, ΔT_3 with data from literature and use the experimental and computational values of h_{df} for ΔT_4. The fuel temperature can be computed directly by using visualization application (for example ParaView application) [27, 30]. The fuel temperature can be obtained in any point of the fuel by using (1.29) where T_f is the temperature computed by the FEM-LCORE application.

Pressure loss source. In a similar way the pressure drop distribution must be reported in the `axlpf` matrix and in the `axllf` vector. The `axlpf` matrix defines

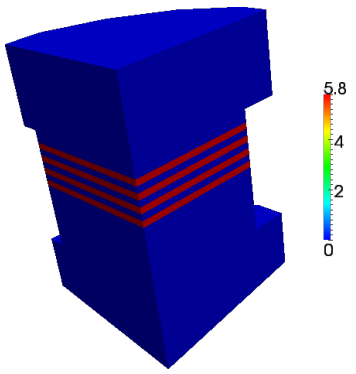

Figure 1.9: Pressure loss source

the pressure losses in each assembly as

$$\begin{array}{c} A1 \\ A2 \\ A3 \\ A4 \\ A5 \\ A6 \\ A7 \\ A8 \\ 1 \end{array} \begin{bmatrix} \beta_{A1_1} & \beta_{A1_2} & \beta_{A1_3} & \beta_{A1_4} & \beta_{A1_5} & \beta_{A1_6} & \beta_{A1_7} & \beta_{A1_8} \\ \beta_{A2_1} & \beta_{A2_2} & \beta_{A2_3} & \beta_{A2_4} & \beta_{A2_5} & \beta_{A2_6} & \beta_{A2_7} & \beta_{A2_8} \\ \beta_{A3_1} & \beta_{A3_2} & \beta_{A3_3} & \beta_{A3_4} & \beta_{A3_5} & \beta_{A3_6} & \beta_{A3_7} & \beta_{A3_8} \\ \beta_{A4_1} & \beta_{A4_2} & \beta_{A4_3} & \beta_{A4_4} & \beta_{A4_5} & \beta_{A4_6} & \beta_{A4_7} & \beta_{A4_8} \\ \beta_{A5_1} & \beta_{A5_2} & \beta_{A5_3} & \beta_{A5_4} & \beta_{A5_5} & \beta_{A5_6} & \beta_{A5_7} & \beta_{A5_8} \\ \beta_{A6_1} & \beta_{A6_2} & \beta_{A6_3} & \beta_{A6_4} & \beta_{A6_5} & \beta_{A6_6} & \beta_{A6_7} & \beta_{A6_8} \\ \beta_{A7_1} & \beta_{A7_2} & \beta_{A7_3} & \beta_{A7_4} & \beta_{A7_5} & \beta_{A7_6} & \beta_{A7_7} & \beta_{A7_8} \\ \beta_{A8_1} & \beta_{A8_2} & \beta_{A8_3} & \beta_{A8_4} & \beta_{A8_5} & \beta_{A8_6} & \beta_{A8_7} & \beta_{A8_8} \end{bmatrix} \\ \begin{array}{cccccccc} 1 & 2 & 3 & 4 & 5 & 6 & 7 & 8 \end{array}$$

The vertical pressure loss factor can be assumed to have any distribution $q(z)$. This discrete profile is written in the `axpf` array as

$$\begin{array}{c} \\ \\ \\ \\ \\ \\ \\ height \end{array} \begin{bmatrix} Z_1 & q_I(Z_1) & q_O(Z_1) \\ Z_2 & q_I(Z_2) & q_O(Z_2) \\ Z_3 & q_I(Z_3) & q_O(Z_3) \\ Z_4 & q_I(Z_4) & q_O(Z_4) \\ Z_5 & q_I(Z_5) & q_O(Z_5) \\ Z_6 & q_I(Z_6) & q_O(Z_6) \end{bmatrix} \begin{array}{c} \\ \\ \\ \\ \\ \\ \\ I \end{array} \begin{array}{c} \\ \\ \\ \\ \\ \\ \\ O \end{array} \tag{1.30}$$

where Z_i are the discrete vertical coordinates and $q0$ and $q1$ are the values in the INNER and OUTER zones. The pressure loss distribution defined by the grid in Figure 1.6 can be easily written by defining the modulus of the vector function $|\bar{\beta}|$ where the discrete pressure drops are defined by

$$\frac{1}{2}\bar{\beta}(\mathbf{x}) \cdot \mathbf{v}|\mathbf{v}|\,. \tag{1.31}$$

If we assume the flow to be approximately vertical then $\bar{\beta}(\mathbf{x}) \cdot \mathbf{v}|\mathbf{v}|/2 = |\bar{\beta}||\mathbf{v}|^2/2$. This is the result of the usual mono-dimensional approximation.

1.5 1D-porous scale (component system scale)

1.5.1 Model description

The 1D-porous module used in FEM-LCORE is simply obtained by integrating (1.25-1.27) with the right weight functions. For details see [7, 8, 9]. This module is properly used for mono-dimensional flows inside complex components.

1D-CFD mass equation. In this case we have

$$\int_0^L \psi(s)\,\frac{\partial}{\partial s}\,(\bar{r}\,\bar{\rho}\,\bar{\hat{v}}\,A)\,ds = 0 \quad \forall \psi \in P(0,L)\,. \tag{1.32}$$

1D-porous momentum equation. In a similar way for the average quantities ($\bar{\rho}$, $\bar{v}$, $\bar{p}$) and $\phi \to \phi(s)$ we have for the momentum mono-dimensional equation

$$\begin{aligned}\int_0^L (\frac{\partial}{\partial t}\,\bar{r}\,\bar{\rho}\,\bar{v}\,A)\,\phi(s)\,ds + \int_0^L \bar{r}\,\bar{\rho}\,A\,\bar{v}(\frac{\partial}{\partial s}\bar{v})\,\phi\,ds = \int_0^L (\bar{r}\bar{p}+\bar{p}_l)\,A\,\frac{\partial}{\partial s}\,\phi\,ds \\ \int_0^L \bar{r}\,A\bar{\rho}\mathbf{g}\cdot\widehat{i}_s\,\phi\,ds + \int_0^L \phi(s)\,(\bar{r}M_v)\,ds \qquad \forall \phi \in V(0,L)\,,\end{aligned} \tag{1.33}$$

where M_v is the volume contribution. The volume contribution M_v consists of several terms. We have $M_v = M_{v,vv}(\bar{\mathbf{v}}\bar{\mathbf{v}} - \bar{v}\bar{v}) + M_{v,\widehat{\tau}}(\bar{\tau}) + M_{v,\widehat{\tau}^{\tau}}(\bar{\tau}^{\tau}) + M_{v,\widehat{\tau}^{eff}}(\bar{\tau}^{eff})$ with obvious definition of the terms.

1D-porous energy equation. For the Energy equation the average quantities involved are ($\bar{\rho}$, $\bar{v}$, $\bar{p}$, $\bar{T}$) and the equation becomes

$$\begin{aligned}\int_0^L \frac{\partial\,\bar{r}\,A\,\bar{\rho}\,C_p\,\bar{T}}{\partial t}\,\varphi(s)\,ds + \int_0^L \frac{\partial}{\partial s}\,(\,\bar{r}\,A\,\bar{\rho}\,\bar{v}C_p\,\bar{T})\,\varphi\,ds = \\ -\int_0^L (\bar{r}\,Q_v + Q_s)\,\varphi\,d\mathbf{x} \quad \forall \varphi \in \mathbf{H}(\Omega)\,.\end{aligned} \tag{1.34}$$

We have contributions from the boundary and contributions from the volume. From surface integrals (surface interaction) we define Q_s as

$$Q_s = Q_{s,q}(\mathbf{q}) + Q_{s,v}(\,\vec{v}\cdot\mathbf{n}\,\bar{T}) \tag{1.35}$$

with $Q_{s,v}(\vec{v}\cdot\mathbf{n}\,\bar{T}) \approx 0$ and $Q_{s,q} \approx Q_{int}$ (heat exchange through surfaces). From volume integral (volume interaction) we define

$$Q_v = Q_{v,q}(\bar{\tau}) + Q_{v,vv}(\bar{\mathbf{v}}\bar{\mathbf{T}} - \bar{v}\bar{T}) + Q_{v,\Phi}(\Phi) \tag{1.36}$$

with $Q_{v,q}$ internal heat conduction and $Q_{v,vv}$ turbulent term. For details see [7, 8].

1D-porous scale model. In standard form (non variational form) the 1D-porous scale model, defined by (1.32-1.34), can be written as the following system

$$\frac{\partial}{\partial s}\big(\,\bar{r}\;\bar{\rho}\,\bar{v}\,A\big) = 0\,, \tag{1.37}$$

$$\frac{\partial}{\partial t}\;\bar{r}\,A\bar{\rho}\bar{v} + \;\bar{r}\,\bar{\rho}\,A\,\bar{v}\,\frac{\partial}{\partial s}\big(\bar{v}\big) + \;A\,\frac{\partial}{\partial s}\,P = -\,\beta\,\frac{\bar{\rho}}{2}\,\bar{v}|\bar{v}| + \;\bar{r}\,\bar{\rho}\,A\,g_s + \;\bar{r}\,M_v\,, \tag{1.38}$$

$$\frac{\partial}{\partial t}\,\bar{r}\,A\,\bar{\rho}\,C_p\,\bar{T} + \frac{\partial}{\partial s}\,\bar{r}\;A\,\bar{\rho}\,\bar{v}\,C_p\,\bar{T} = \;\bar{r}\,\rho\,A\,\bar{v}\,g_s + \bar{Q}_s + \bar{Q}_v\,. \tag{1.39}$$

The first equation states that the mass flux $\dot{m} = \bar{r}\bar{\rho}\,\bar{v}\,A$ is constant in space even if it can change in time. If $\bar{r}$ is constant, as usual, also the total mass flux $\bar{\rho}\,\bar{v}\,A$ is constant. If the density is a function of temperature then the average velocity $\bar{v}$ must change in agreement with the density change.

1.5.2 1D-porous module for primary loop

Equation model. The primary loop contains the heat exchanger and it is of fundamental importance for the dynamics of the system. In order to simplify the computation we model this part of the nuclear reactor by using a simple 1D-porous modulus. In this work we use a 1D-porous modulus built inside the code itself but we

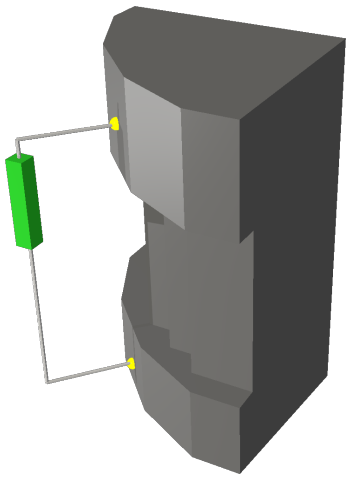

Figure 1.10: Schematic of 1D-porous module

plan in the future to allow coupling with external code such as CATHARE through the platform SALOME. The 1D-porous module consists of the following equations

- mass conservation equation defined in (1.37);
- momentum conservation equation defined in (1.38),

- energy equation defined in (1.39).

In order to simplify the solution of the system (1.37-1.39) we use the mass flux variable instead of the velocity field. We set

$$\bar{m} = \bar{r}\ \bar{\rho}\,\bar{v}\,A\,. \tag{1.40}$$

The new set of equation is

$$\frac{\partial}{\partial s}(\bar{m}) = 0\,, \tag{1.41}$$

$$\frac{\partial}{\partial t}\bar{m} + \bar{m}\,\frac{\partial}{\partial s}(\bar{v}) + A\,\frac{\partial}{\partial s}P = -\beta\,\frac{\rho}{2}\,\bar{v}|\bar{v}| + \bar{\rho}\,A\,g_s + \bar{r}\,M_v + M_s\,, \tag{1.42}$$

$$\frac{\partial}{\partial t}A\,\bar{\rho}\,C_p\,\bar{T} + \frac{\partial}{\partial s}\,\bar{m}\,C_p\,\bar{T} = \rho\,A\,\bar{v}\,g_s + \bar{Q}_s + \bar{r}\,\bar{Q}_v\,. \tag{1.43}$$

The solution of the first equation imposes that $\bar{m}$ is constant along all the mono-dimensional path. In order to model different situations we can consider A and $\bar{r}$ as a function of the mono-dimensional space variable s. In this way a section or material changing can be taken into account.

Steam Generator (SG) model. Due to computational limitations and unknown geometrical details of the involved structures it is very hard to solve in details a three-dimensional model of the heat exchanger. A simplified 1D-porous module must be used instead. The 1D-porous module describes the heat exchanger through volumetric source terms. In standard operation conditions, the liquid flow enters the steam generator units with inlet temperature $\bar{T}_{i,sg}$ and exit at outlet temperature $\bar{T}_{o,sg}$. The formulation of the steam generator heat sink is of main interest for the LF reactor, as it is used for establishing the temperature level of the primary loops.

The secondary system is operating with a fluid at fixed temperature $T_{min,sg}$ which is the minimum temperature that the core can attains. In this work we consider one simple model: a linear dependency of the heat flux based on the two fixed temperatures at inlet and outlet of the steam generator. In the (1.43) the volumetric term Q_s is defined as

$$Q_s = \begin{cases} -k_{sg}(T - T_{min}) & \bar{T}_{sg} > T_{min} \\ 0 & T_{sg} < T_{min} \end{cases}\,, \tag{1.44}$$

where k_{sg} is the heat power per unit of temperature degree and SG volume subtracted from the steam generator and $\bar{T}_{sg}$ the averaged lead temperature at the SG inlet. In a simplify version of this model we may set T_{min} and assume that the steam generator gives fixed temperature at the inlet of the reactor.

The stem generator are treated as porous media with a porosity of r for the SG core region. The distributed pressure loss are computed in (1.42) by defining the β coefficient. The accidental pressure losses in the inner/outer SG generator are uncertain and they will be ignored even if this could become important in the free convection conditions with low flow rates. If the pumps are switched off and the decay heat production of the core becomes the driving force due to different densities. then the design of the steam generator and its accidental pressure losses become the limiting factor of the natural convection flow rate.

Pump (P) model. The pump is taken into account with a simple constant volume term. In our module we set

$$M_v = \Delta P\,, \tag{1.45}$$

where ΔP is the pressure gained by the pump for the unit of length in the flow direction.

1.6 Module interfaces

1.6.1 3D-CFD/3D-porous interface

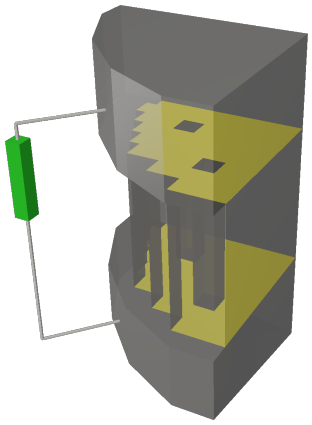

Figure 1.11: 3D-CFD/3D-porous interfaces in a reactor model schematic diagram.

As shown in Figure 1.11 the 3D-CFD/3D-porous interfaces are the inlet and the outlet of the core. The core inlet, shown in yellow, is the interface between the lower plenum and the core while the core outlet is the interface between the upper plenum and the core. At these interfaces the fluid must flow from one module to the other and conserve the momentum. The 3D-CFD module in the plenum is different from the 3D-porous module since in the porous model the fluid and solid material are together inside the considered volume. The fluid flow is clearly reduced with respect

to the total area. The flow reduction is defined by the volume ratios

$$\zeta = \frac{V_m}{V_{tot}} \quad r = 1 - \zeta \tag{1.46}$$

where ζ and r are the ratio between no-fluid material and total volume and between fluid and total volume, respectively. The problem of the continuity of the velocity field through the interface 3D-CFD/3D-porous modules can be solved by defining a new velocity field variable

$$\widehat{\mathbf{v}}^* = \widehat{\mathbf{v}} \quad \text{3D-CFD} \tag{1.47}$$

$$\widehat{\mathbf{v}}^* = r\,\widehat{\mathbf{v}} \quad \text{3D-porous}\,. \tag{1.48}$$

With this definition the system (1.25-1.26) becomes

$$\nabla \cdot \rho\,\widehat{\mathbf{v}}^* = 0 \tag{1.49}$$

$$\frac{\partial \rho\,\widehat{\mathbf{v}}^*}{\partial t} + (\nabla \cdot \rho\,\widehat{\mathbf{v}}^*\widehat{\mathbf{v}}) = -\nabla(\widehat{p} + \widehat{p}_l) + \nabla \cdot (\widehat{\tau}^* + \widehat{\tau}^{*\tau} + \widehat{\tau}^{*eff}) + \rho\mathbf{g} \tag{1.50}$$

The system (1.49-1.50) is valid in the plenum and in the core region and maintain velocity and pressure fields continuous. The temperature field remains continuous at the 3D-CFD/3D-porous interface and therefore the equation (1.27) can be applied in both regions with the appropriate value of r and the corresponding coefficients.

With this approach the use of a unique equation in both region allows a strong and robust coupling between the velocity pressure and temperature fields.

1.6.2 Interface 3D/1D-3D/1D porous

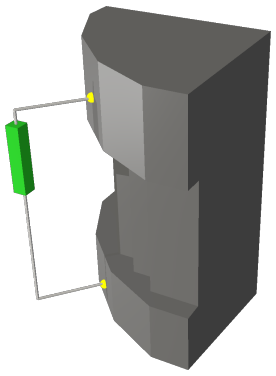

Figure 1.12: 3D-CFD/1D-porous interfaces in a reactor model schematic diagram

As shown in Figure 1.12 the 3D-CFD/1D-porous interfaces are the inlet and the outlet of the plenum regions. The lower plenum inlet, shown as yellow sphere, is the interface between the lower plenum and the primary loop while the plenum outlet is the interface between the upper plenum and the primary loop. At these interfaces

the fluid must flow from one-dimensional module to a three-dimensional one. In this interface the mass, momentum and the temperature field must be conserved. There are many sophisticated techniques to define a numerical algorithm able to identify the values to set on the interfaces for example one can use algorithms based on Mortar or Lagrangian multiplier method but here we use a very simple approach.

The one-dimensional module is essentially a hyperbolic differential equation and therefore it requires boundary conditions only in inflow regions. The interface 1D-porous/3D-CFD that links the 1D-porous module to 3D-CFD module of the lower plenum is an outflow region for the reactor and therefore it does not require boundary conditions. The surface of the lower plenum is an inlet region for the core/plenum system and therefore the average temperature, velocity and pressure must set as boundary conditions. This is a very challenging situations. From the mono-dimensional primary loop we have the mass flux (or velocity in the normal direction), pressure and temperature. In three-dimensional domains if the vector of the velocity is fully specified on boundaries then the pressure is determined. The pressure can be specified only if the normal component of the velocity field is not imposed. Imposing pressure with brute force on the inlet surface leads to large oscillations and velocity discontinuities. For this reason we compute, with a non linear algorithm, the velocity field that matches the pressure of the plenum and the primary loop. The velocity field is kept continuous and the two pressures (in the plenum and in the primary loop) matches iteratively. This approach substantially reduces the time step of the core/plenum system to 1/4 or 1/5 of the step of the primary loop.

Chapter 2

Numerical Results: natural convection

2.1 Reactor model

2.1.1 Geometrical model

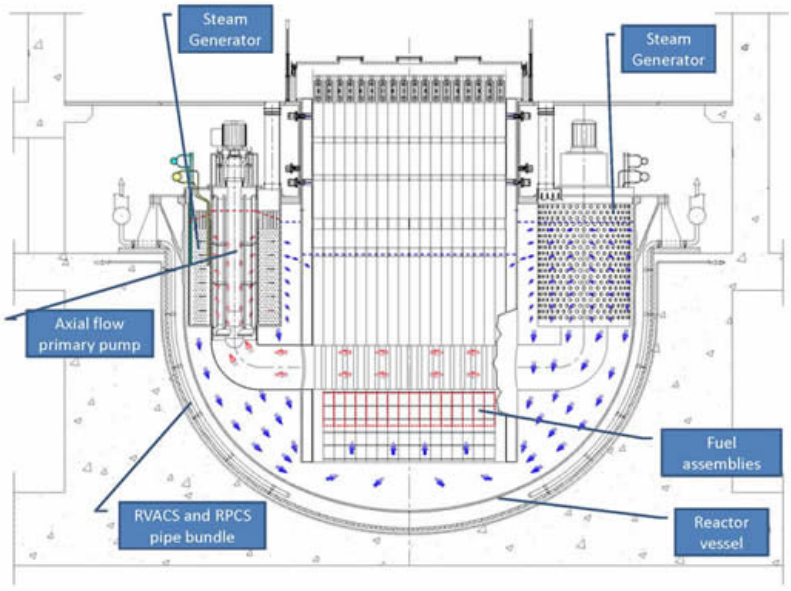

Figure 2.1: Schematic of the reactor.

The LFR model for these computations is the type-pool LFR reactor ELSY, shown in Figure 2.1. The nuclear reactor ELSY (European Lead-cooled System) is characterized by a very compact design and its main characteristics are illustrated in Table 2.1. One of main important aspect of this reactor is that it uses lead as basic coolant. This is due to its good chemical behavior and its thermodynamic

Parameters	ELSY
Power [MWe]	600
Conversion Ratio	1
Thermal efficiency [%]	42
Primary coolant	Lead
Primary coolant circulation	Forced
Primary coolant circulation for DHR	Natural
Core inlet temperature	673.15K
Core outlet temperature	753.15K
Fuel	MOX (Nitrides)
Fuel cladding material	T91 (aluminized)
Peak cladding temperature	823.15K
Fuel pin diameter [mm]	10.5
Active core dimensions	Heigh/diameter [m] 0.9/4.32
Primary pumps	8 integrated in the SG
Working fluid	Water-superheated at 18 MPa, 450°C
Primary/secondary heat transfer system	8 Pb-to-H2O SGs
Direct heat removal (DHR)	Reactor Vessel Air Cooling System + 4 Direct Reactor Cooling Systems + 4 Secondary Loops Cooling Systems

Table 2.1: Main characteristics of the ELSY reactor.

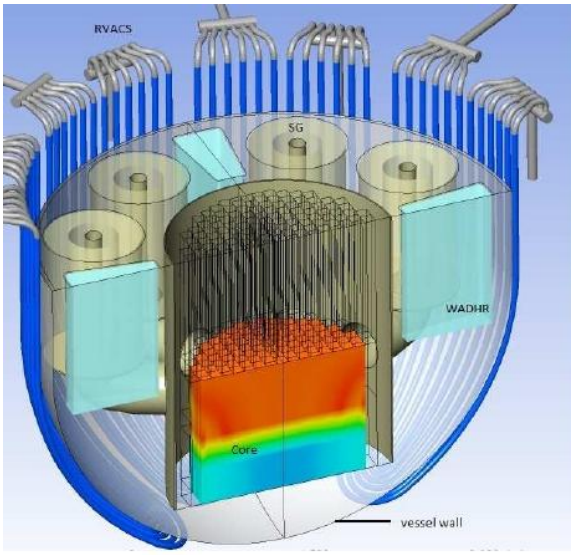

Figure 2.2: Schematic of the main components of the reactor.

properties. The main disadvantages of this coolant are the high solidification temperature of $600.15K$ and the oxidation and corrosion behavior. The thermal power of one unit at nominal conditions is $1500MW$ at a total mass flow rate of about

$126000Kg/s$. The LFR vessel has 8 primary loops with 8 steam generators (SG) and 8 integrated primary pumps. At nominal conditions the coolant enters the core at $T = 673.15K$ to reach the outlet at temperature of about $753.15K$. For the secondary loop superheated water-steam is used to reach a thermal efficiency of about 43%. This converts the $1500MW$ heat power into $600MW$ of electrical power. A simple schematic, with the main components, can be seen in Figure 2.2. A detailed description of the ELSY reactor is presented in [2, 4].

As shown in Figure 2.3 we consider the LFR system basically divided into three

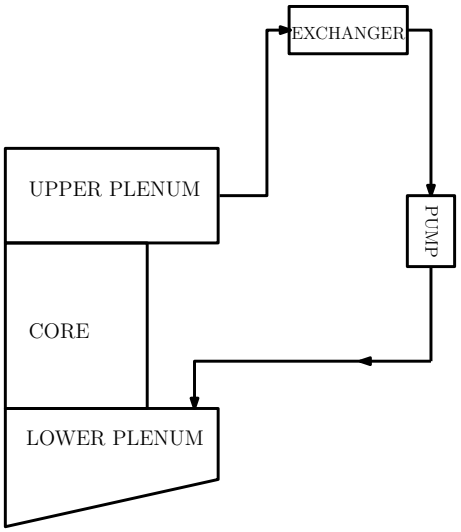

Component	scale	Dimension	Module
Plenum	CFD scale	3D	3D-CFD
Core	porous scale	3D	3D-porous
Primary heat exchange loop	system scale	3D	1D-porous

Figure 2.3: Modules used in the multiscale LFR modelization.

regions: heat exchange loop (1D-porous), plenum (3D-CFD) and core (3D-porous) region. The computational mesh is shown in Figures 2.4-2.6, with geometrical dimensions taken from Figure 2.5. Let us consider the active (upper) and non-active (lower) core sections and the upper and lower plenum defined as in 2.5. If we set the zero vertical coordinate at the lower point, the core region goes from $1.3m$ to $3.24m$. The active core (upper core) where heat is generated ranges between $H_{in} = 2.25m$ and $H_{out} = 3.15m$. Below the core we have the lower plenum with the inlet between 0 and $H_{lp} = 1.3m$. The lower plenum has an approximate hemispherical form with the lowest region at $H_{bot} = 0$ (reference point). Above the core for a total height of $1.24 = H_{up}m$ there is the upper plenum with the coolant outlet.

The generation of this mesh is not trivial. In fact care must be taken in such a way that every assembly is exactly discretized by entire cells. In this way all the

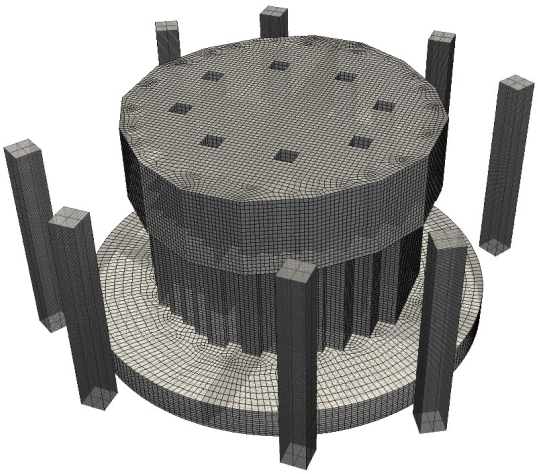

Figure 2.4: Computational domain.

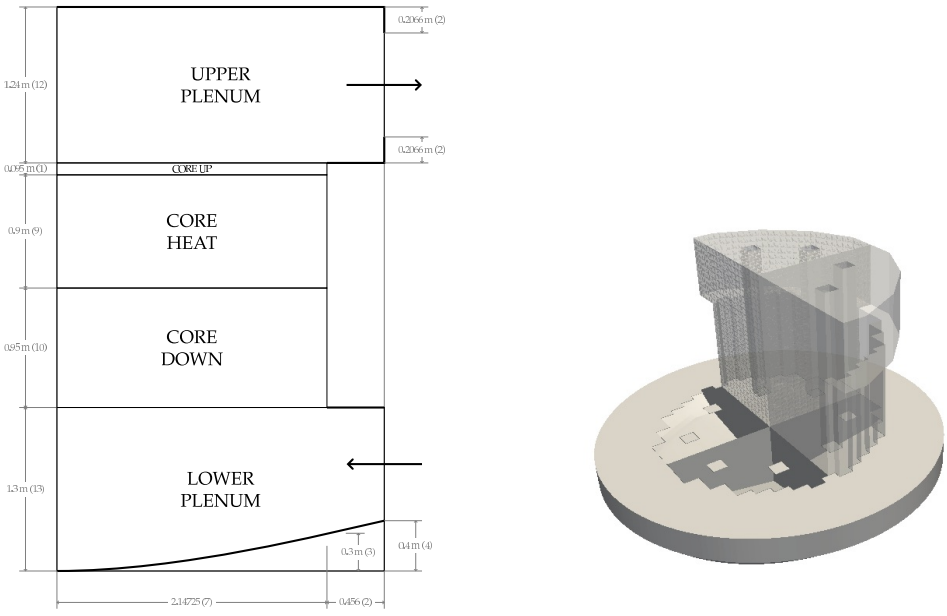

Figure 2.5: Schematic of the reactor core and plenum section and upper plenum computational domain.

data attributes related to a given assembly may be easily associated. For details we refer to [8].

In the design of this LFR reactor there are 8 primary loops. Each of them contains a steam generator and a pump. We model each of this reactor segment as a 1D-porous module. The schematic of this module is defined in Figures 2.7 where

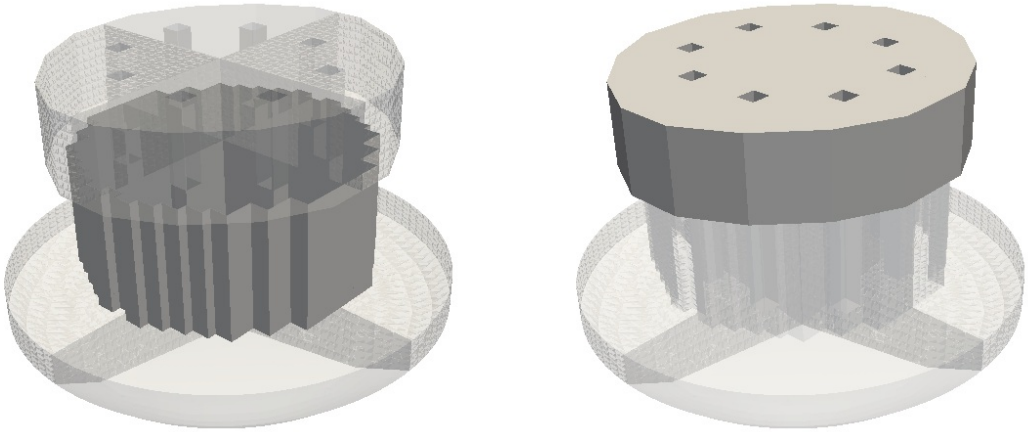

Figure 2.6: Core and lower plenum computational domain.

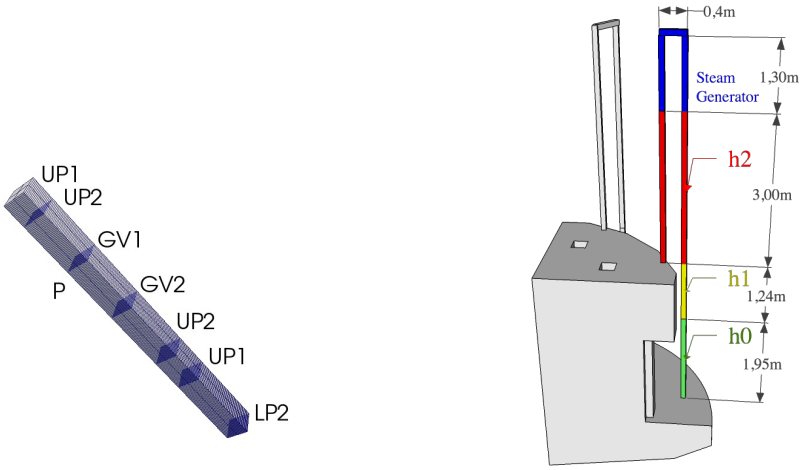

Figure 2.7: Schematic of primary loop with heat exchanger.

along the mono-dimensional module (left) one can find the upper plenum from UP1 to UP2, the steam generator from GV1 and GV2 together with the pump P. The point with label LP2 indicates the entrance in the lower plenum. Since the interface between the 3D and 1D module is defined by a single point, the primary loop starts at the lower point of the upper plenum outlet and ends at the upper point of the lower plenum inlet on the right part of Figure 2.7 we can see the seal path of the primary loop.

2.1.2 Heat core generation model.

The core reactor is divided in assembly as shown in Figure 2.8. Each fuel assembly consists of a $n_p \times n_p = 21 \times 21$ pin lattice. The design of the assembly and its characteristics are shown in Figure 2.9. In particular we note that the coolant/assembly ratio r is 0.548. Each assembly has a square section with a side length of $L = 0.294m$ and this completely defines the horizontal core structure. For the vertical geometry we refer to Figure 2.5 [4, 15, 18, 1].

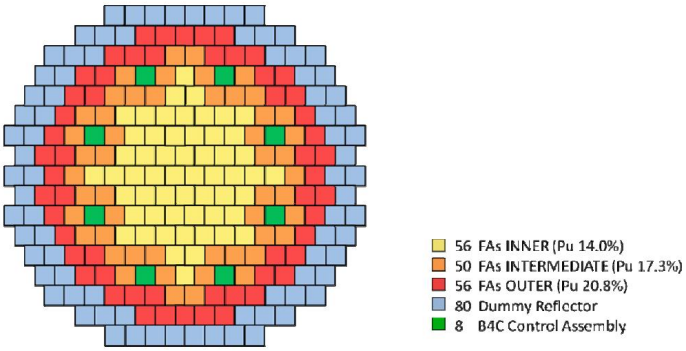

Figure 2.8: Reactor fuel distribution.

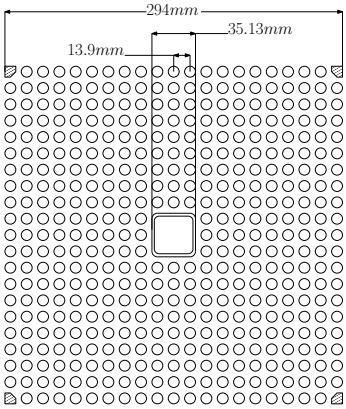

	area (m^2)
Pin area	370.606×10^{-4}
Corner box area	5.717×10^{-4}
Central box beam	2.092×10^{-4}
Channel central box beam area	12.340×10^{-4}
Coolant area	473.605×10^{-4}
Assembly area	864.360×10^{-4}
Coolant/Assembly ratio	0.5408

Figure 2.9: Schematic of the assembly and its main characteristics.

Inner		Intermediate		Outer	
A11/2*	8.606	A16/2*	10.775	A17/2*	10.036
A12/2*	8.801	A25	10.188	A27	10.908
A13/2*	9.043	A26	10.269	A28	7.842
A14/2*	9.301	A34	9.943	A37	8.465
A15/2*	9.560	A36	9.249	Aa7	8.520
A21/2*	8.678	A45	10.132	A55	10.962
A22	8.759	A46	9.399	A56	8.621
A23	8.943	A52	9.696	A65	9.766
A24	9.112	A53	9.857	A66	7.776
A3l	8.811	A54	10.400	A72	9.746
A32	8.921	A62	9.410	A73	8.833
A33	9.071	A64	9.057	A74	7.699
A41/2*	8.850	A71	9.318	A81/2*	8.029
A42	8.903			A82	7.806
A43	9.043			A83	6.922
A44	9.218				
A5l	8.790				
A61/2*	8.725				

	Power $MWth$	# FA	Pavg $MWth$	ffrad
Inner	501.41	56	8.95	1.07
Intermediate	489.23	50	9.78	1.10
Outer	491.60	56	8.78	1.25
Total	1482.24	162	9.15	

Table 2.2: Horizontal fuel distribution. The value labeled with star (*) are referred to the entire assembly

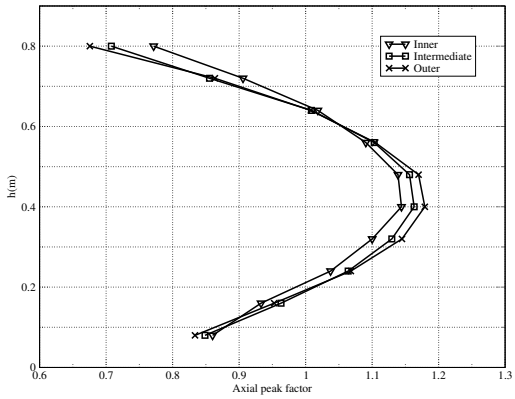

Figure 2.10: Axial fuel distribution

The overall number of assembly positions in the core is 170. Eight of these positions are dedicated to house special control rods and therefore the global number of fuel assemblies is 162. The transverse core area is approximately circular but not axial symmetric. However, we can argue from Figure 2.8 that two symmetry planes passing through the reactor axis can be identified so that only a quarter domain has to be taken into account for the simulations. The model design distributes the fuel assemblies in three radial zones: $N_{a1} = 56$ fuel assemblies in the inner zone, $N_{a2} = 62$ fuel assemblies in the intermediate zone and the remaining $N_{a2} = 44$ fuel assemblies in the outer one. The power distribution factors, i.e. the power of a fuel assembly over the average fuel assembly power, are mapped in Figures 2.2-2.10. The maximum power factor is 1.17, while the minimum is 0.74. In the computational

model the following matrix of fuel pick factor is assumed

$$\begin{array}{c} \\ A1 \\ A2 \\ A3 \\ A4 \\ A5 \\ A6 \\ A7 \\ A8 \\ \\ 1 \end{array} \begin{bmatrix} 0.941 & 0.962 & 0.989 & 1.017 & 1.045 & 1.178 & 1.097 & 0. \\ 0.949 & 0.958 & 0.978 & 0.996 & 1.114 & 1.123 & 1.193 & 0.857 \\ 0.963 & 0.975 & 0.992 & 1.087 & R & 1.011 & 0.925 & 0. \\ 0.967 & 0.973 & 0.989 & 1.008 & 1.108 & 1.028 & 0.931 & 0. \\ 0.961 & 1.060 & 1.078 & 1.137 & 1.198 & 0.943 & 0. & 0. \\ 0.954 & 1.029 & R & 0.990 & 1.068 & 0.850 & 0. & 0. \\ 1.019 & 1.066 & 0.966 & 0.842 & 0. & 0. & 0. & 0. \\ 0.878 & 0.853 & 0.757 & 0. & 0. & 0. & 0. & 0. \end{bmatrix} \begin{array}{c} \\ \\ \\ \\ \\ \\ \\ \\ \\ 2 \quad 3 \quad 4 \quad 5 \quad 6 \quad 7 \quad 8 \end{array}$$

2.1.3 Thermophysical properties

The natural convection flow appears when big differences in temperature drive to big differences in the density. In order to obtain such a motion we have set all properties as a function of temperature . For liquid lead coolant one can refer to [20, 19, 6]. The lead density is assumed to be a function of temperature as

$$\rho = (11367 - 1.1944 \times T)\,\frac{Kg}{m^3} \tag{2.1}$$

for lead in the range $600K < T < 1700K$ [20, 19]. The following correlation is used for the viscosity μ

$$\mu = 4.55 \times 10^{-04}\, e^{(1069/T)}\, Pa \cdot s\,, \tag{2.2}$$

for lead in the range $600K < T < 1500K$ [20, 19]. The reference temperature T_{ref} is the inlet temperature (if fixed), which is assumed always uniform in the lower plenum inlet. In many cases the reference temperature is $T_{ref} = 673.15K$, the inlet temperature in standard working conditions. For the reference temperature T=673.15K the properties are computed in Table 2.3. For the mean coefficient of

properties		value
Density $\rho_0(673.15K)$		$(11367 - 1.1944 \times 673.15) = 10562$
Viscosity $\mu_0(673.15K)$		0.0022
Thermal conductivity $\kappa_0(673.15K)$		$15.8 + 108 \times 10^{-4}\,(673.15 - 600.4) = 16.58$
Heat capacity C_p		147.3

Table 2.3: Lead properties at T=673.15K.

thermal expansion (AISI 316L) we assume

$$\alpha_v = 14.77 \times 10^{-6} + 12.20^{-9}(T - 273.16) + 12.18^{-12}(T - 273.16)^2\,\frac{m^3}{K}\,. \tag{2.3}$$

The lead thermal conductivity κ is

$$\kappa = 15.8 + 108 \times 10^{-4} \, (T - 600.4) \, \frac{W}{m \cdot K} \, . \tag{2.4}$$

The constant pressure specific heat capacity for lead is assumed not to depend on temperature, with a value of

$$C_p = 147.3 \, \frac{J}{Kg \cdot K} \, . \tag{2.5}$$

2.1.4 Steam Generator model.

Due to computational limitations and unknown geometrical details of the exchanging spiral pipe structures it is very hard to solve in details a three-dimensional model of the heat exchanger. The standard operation conditions of the eight steam generator units are with inlet temperature of $753.15K$ and outlet temperature of $673.15K$. At standard conditions each unit removes $187.5MW$ at a coolant flow rate of $15000.75Kg/s$ [16, 17, 14, 13]. The formulation of the steam generator heat sink is of main interest for the LFR reactor, as it is used for establishing the temperature level of the primary loop. The secondary loop operates with super-critical water with a temperature of $T = 608K$ at the inlet, which is therefore the minimum temperature for the system. We consider essentially one simple model with a linear dependency of the heat flux based on the two fixed temperatures at inlet and outlet of the steam generator [16, 17, 14]. The total source heat reads

$$Q_{sg} = \begin{cases} -k(T - T_{min}) & \bar{T}_{sg} > T_{min} \\ 0 & T < T_{min} \end{cases} \, , \tag{2.6}$$

where k is given by $187.7MW/145K = 1.29MW/K$ and $\bar{T}_{sg}$ the averaged lead temperature at the SG inlet. In order to simplify further this model we may set $T_{min} = 673.15K$ and assume that the steam generator gives fixed temperature at the inlet of the reactor. The SGs are treated as porous media with a porosity of 0.65 for the core region. Since the accidental pressure loss in the steam generator are difficult to determine we neglect them in this first step approximation. However, as already said if the pumps are switched off and the decay heat production of the core becomes the driving force due to different densities, then the design of the steam generator and its accidental pressure losses become the limiting factor of the natural convection flow rate.

2.2 Test 1. Natural convection with 1500MWth power

This first test simulates the evolution of the system when the pumps are switched off and the heat source of the reactor is kept in standard working conditions. This test allows us to evaluate the nature of the natural convection and the temperature that can be reached in the system. In Figure 2.11 we see the reactor and its reference points. The left and right outlet surface of the upper plenum are labeled with A and B respectively. The points over the inlet of the lower plenum are indicated with D. We have D_1 below the A surface and D_2 below the B surface. The points on the horizontal plane at $z = 3\,m$ in the core are labeled by C . The point C_1 is located in the assembly $A11$, the point C_3 in the assembly $A54$, C_2 in $A26$ and C_4 in $A62$. The points L_1, L_2 and L_3 indicate the location of the vertical lines along the diagonal of the upper plenum.

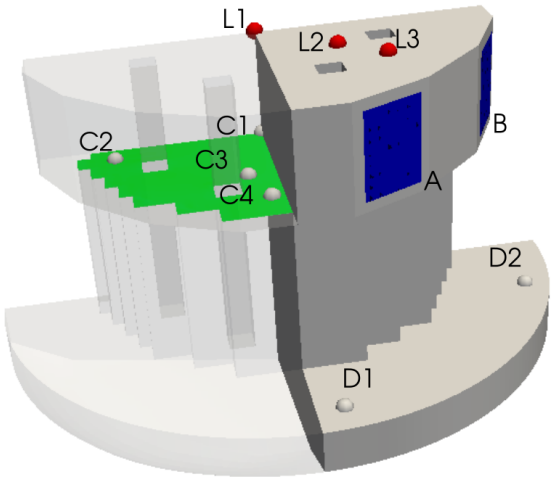

Figure 2.11: Test 1. Geometry and reference points.

2.2.1 Initial conditions

In Test 1 the initial conditions of the reactor is a steady solution in fully working condition with core average velocity of about $\bar{v} = 1.56 m/s$. The corresponding average reduced velocity $\bar{v}^*$ is $\simeq 0.85$ with $r = 0.548$. The non-dimensional mass flux $m^* = m/\rho_0 A$ in the left outlet of the upper plenum is 1.24886 and the corresponding mass flux $m \simeq 16150 Kg/s$ ($A \simeq 1.23 m$ and $\rho_0 = 10563 Kg/m^3$). Since there are 4×2 exits the total mass flux is $\simeq 128000 Kg/s$. We remark that the mass flux

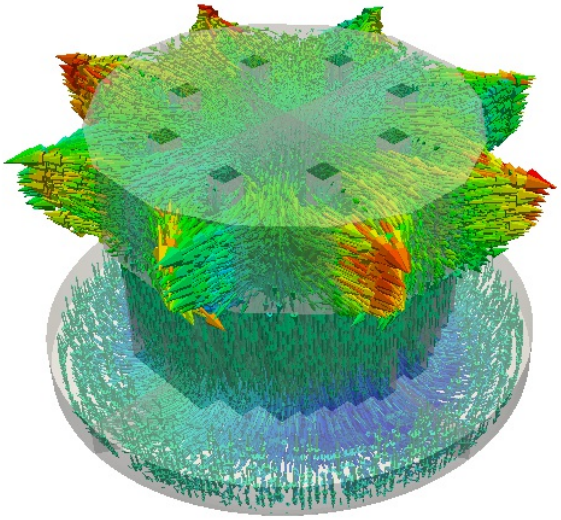

Figure 2.12: Test 1. Reduced velocity field in the reactor and plenum at $t = 0$.

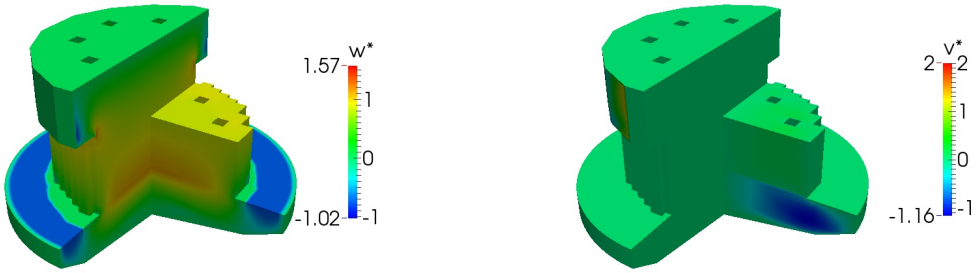

Figure 2.13: Test 1. The w and v-component of the reduced velocity field in the reactor at $t = 0$.

of the left and right outlet of the upper plenum are slightly different due to the fact that the reactor is not symmetric with respect to the diagonal. The velocity field of the initial solution is shown in Figure 2.12. In Figures 2.13-2.14 the three components w,v and u of the reduced velocity field are shown in the various part of the reactor at the initial time. The u and v component of the velocity field have a strong component in the lower plenum and almost vanishing inside the core to gain again its value in the upper plenum. In Figure 2.13 we note that the inlet velocity of the lower plenum is vertical and uniform with value set to $w = w^* = -1.02m/s$. The inlet velocity boundary conditions are defined by the primary loop velocity based on pressure values. The primary loop variables are defined as a unique point since

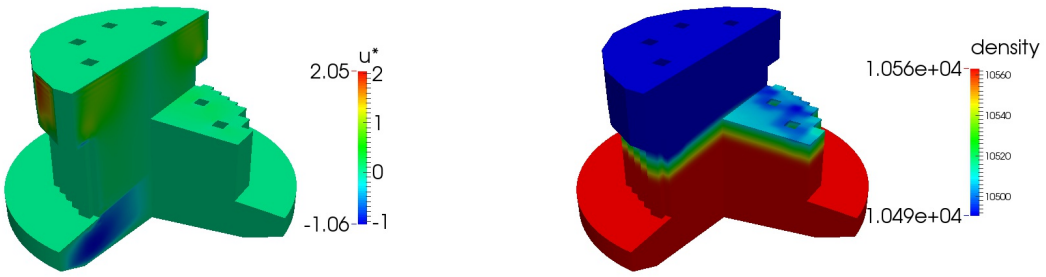

Figure 2.14: Test 1. The u-component of the reduced velocity field and density in the reactor at $t = 0$.

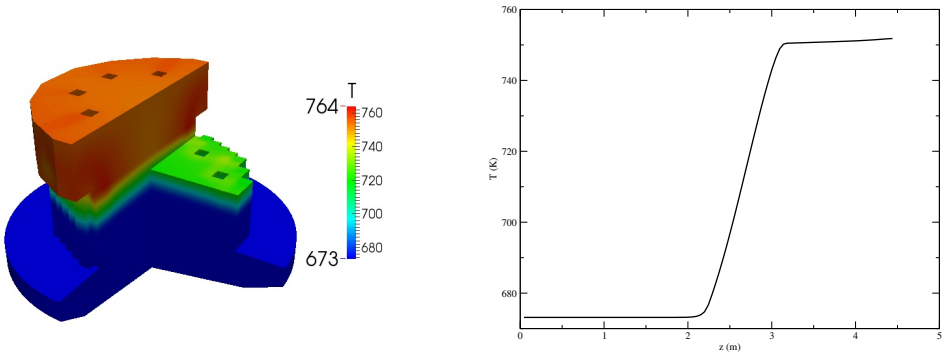

Figure 2.15: Test 1. Temperature distribution in the reactor (left) and along the vertical at the center of the reactor (right) at time $t = 0$.

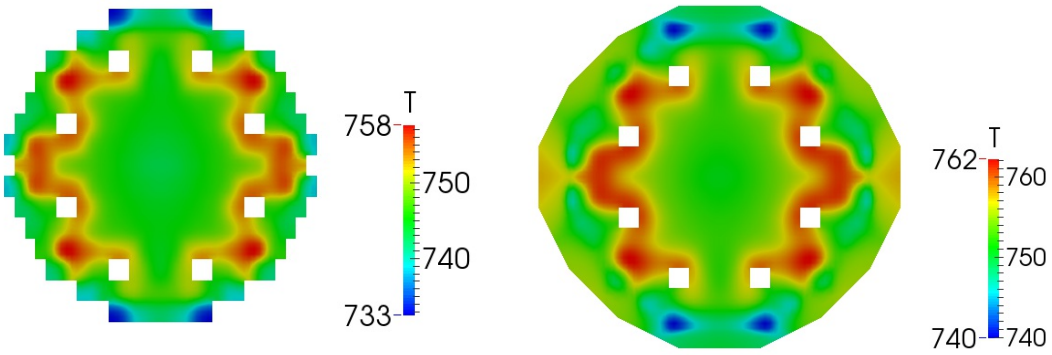

Figure 2.16: Test 1. Temperature distribution over the plane at $z = 3m$ (left) and $z = 3.3m$ (right) at time $t = 0$.

the 1D-porous module is mono-dimensional.

In Figure 2.15 the temperature distribution in the reactor at the initial time is shown. On the left of Figure 2.15 the temperature distribution is over all the reactor.

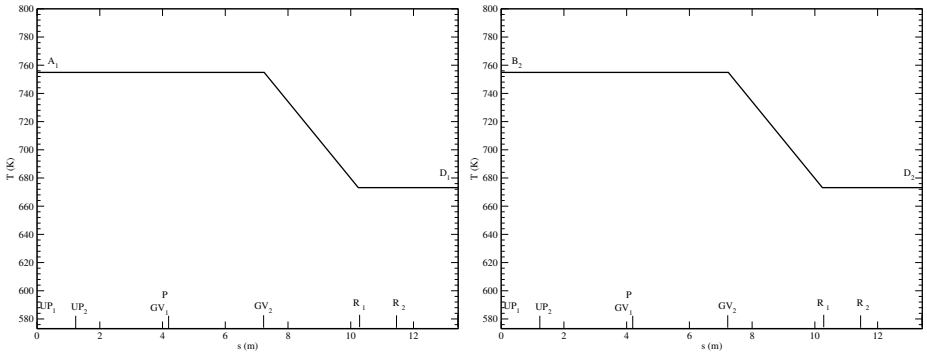

Figure 2.17: Test 1. Temperature distribution in the primary loop A-D (left) and B-D (right) at time $t = 0$.

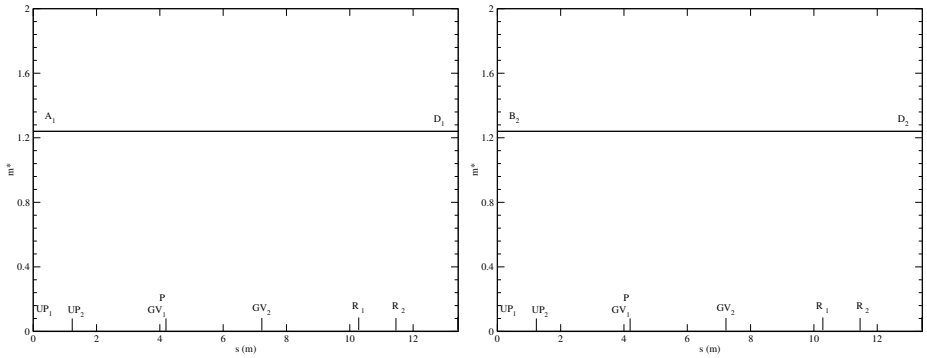

Figure 2.18: Test 1. Non-dimensional mass flux m^* in the primary loop A-D (left) and B-D (right) at time $t = 0$.

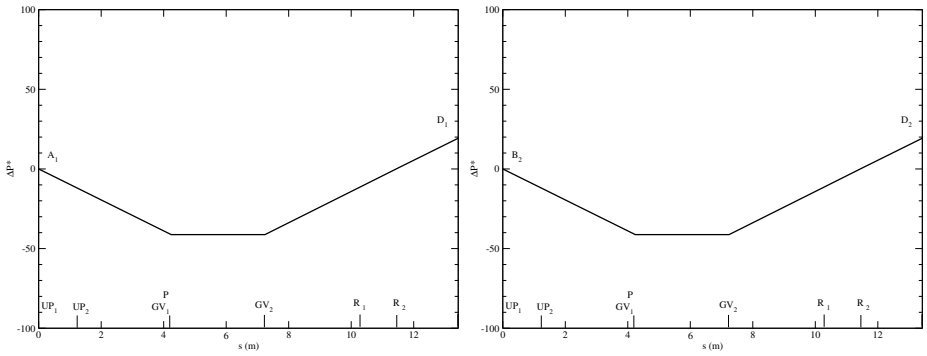

Figure 2.19: Test 1. Non-dimensional ΔP^* in the primary loop A-D (left) and B-D (right) at time $t = 0$.

The average temperature T_{in} over the inlet is $673.15K$ and average temperature in the left and right outlet of the upper plenum is $T_{out} = 754.9K$ for a inlet/outlet temperature difference of $81.75K$. In Figure 2.16 the temperature distribution over the plane at $z = 3m$ (left) and $z = 3.3m$ (right) at time $t = 0$ sec are shown. Over the plane at $z = 3m$ (core exit) the maximum temperature is near the assembly with

higher peak factor. Over the plane obtained by a cut at $z = 3.3m$ the maximum temperature ($762K$) is in the region between the left and right exit of the upper plenum where a stagnation zone does not allow efficient cooling.

In Figures 2.17-2.19 the temperature, pressure and mass flux initial conditions are shown in the primary loop for the branch A-D (left) and B-D (right) as a function of the local mono-dimensional coordinate system. The GV_1 and GV_2 labels refer to the steam generator. In the steam generator area GV_1-GV_2 the gravity is neglected.

2.2.2 Reactor evolution in natural convection flow

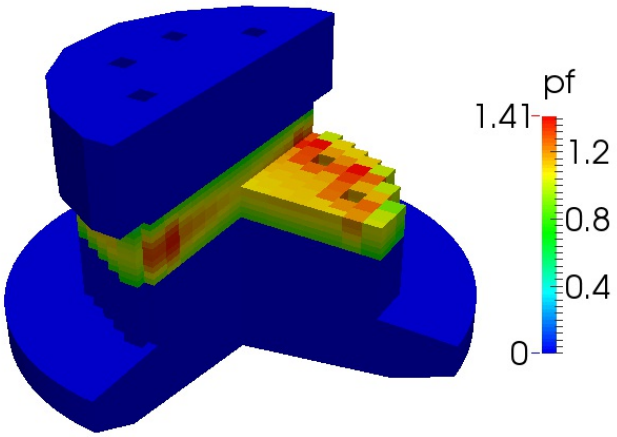

Figure 2.20: Test 1. Power distribution for $t > 0$.

After the initial time the pumps are switched off and the system is moved only by natural convection. The distribution of power remains the same as shown in Figure 2.20. In Figure 2.21 one can see the average temperature $\bar{T}$ and non-dimensional mass flux m^* on left exit surface A and on the right exit surface B as a function of time. The average temperature is reported on the left where, after the the pumps are off, it easy to note that there is a substantial increase to reach constant value after $30s$. The difference between the surface A and B is not large but it implies that the system is not symmetric with respect to the diagonal and it is fully three-dimensional. The non-dimensional mass flux $m^* = m/\rho_0 A$ is reported on right of Figure 2.21. We recall that the area $A \simeq 1.23m$ and $\rho_0 = 10563Kg/m^3$. Due to the lack of pump pressure the mass flux drops to a constant value, which is 1/3 of the nominal mass flux, after approximately after $30s$.

In Figure 2.22 the temperature and the reduced w-component of the velocity field is reported on the point D_1 and D_2 as a function of time. The points D_1 and

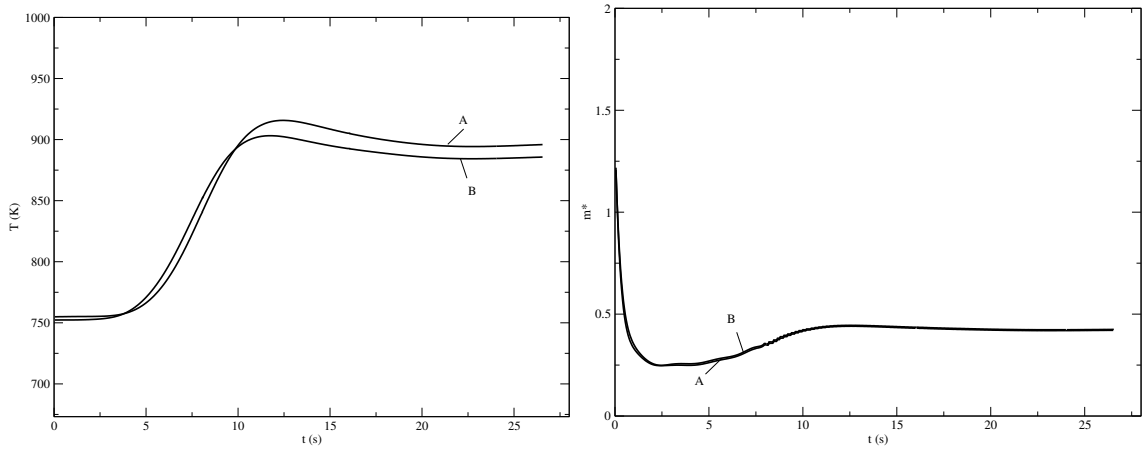

Figure 2.21: Test 1. Average temperature (left) and mass flux $m^* = m/\rho_0 A$ (right) on left exit surface A and on the right exit surface B as a function of time.

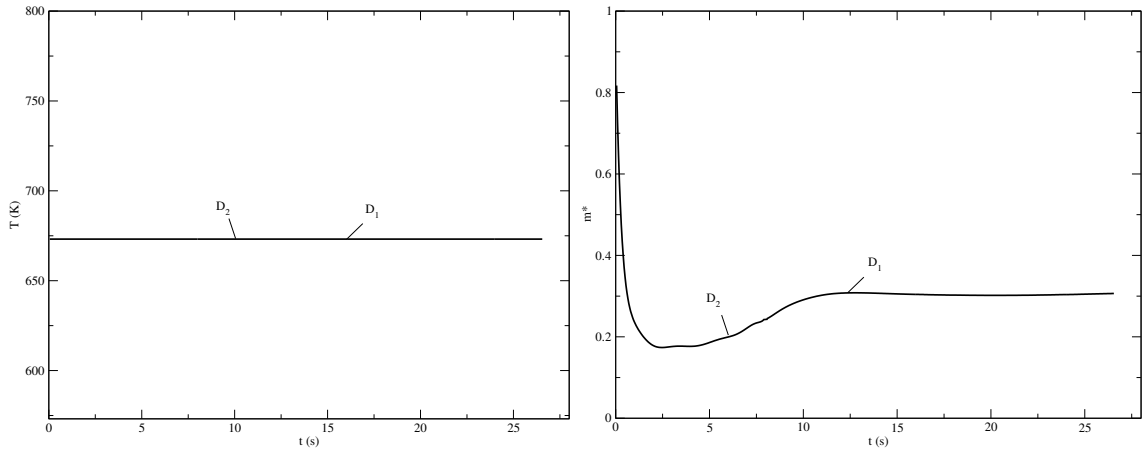

Figure 2.22: Test 1. Temperature (left) and velocity w^* (right) on D_1 and D_2 as a function of time.

D_2 are located in the inlet of the lower plenum. The values are the same since the boundary conditions are imposed uniformly from the primary loop. We recall that $m^* = v^*$ if the temperature is the reactor inlet temperature $673.15K$ and the density is the reference density ρ_0. Streamlines from different points of the lower plenum inlet at $t = 26s$ can be seen in Figure 2.23. From the point D_1 the streamline reaches mainly the exit surface A while from the point D_2 the streamline reaches mainly the exit surface B. Vortexes due to natural convection can be seen in the interior part of the reactor.

The non dimensional pressure drop $\Delta P^* = p^* - p_{ref}$ on D_1 and D_2 is shown as a function of time in Figure 2.24. The non-dimensional pressure is defined by $p/\rho_{ref}\, u_{ref}$ where $\rho_{ref} = \rho_0 = \rho(673.15K)$. The reference pressure p_{ref} is the value of the pressure at the lowest point of the upper plenum exit. The non-dimensional

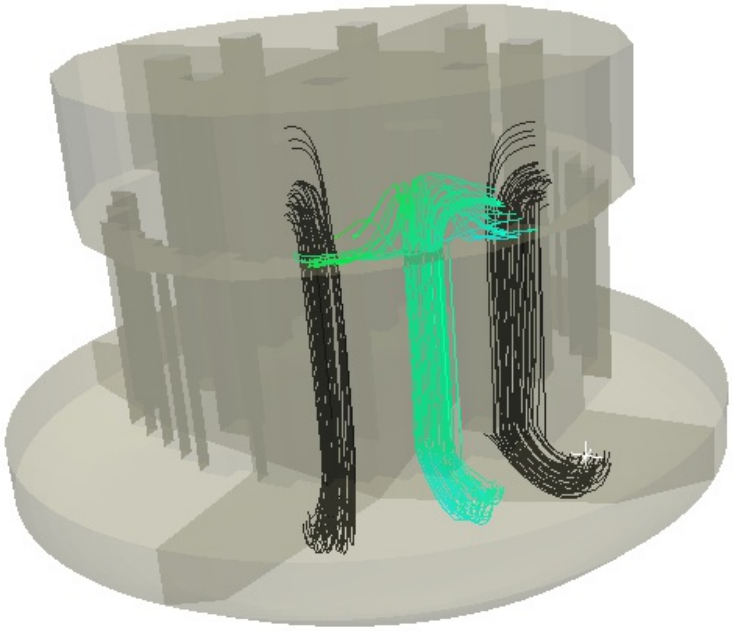

Figure 2.23: Test 1. Streamlines from different point of inlet of the lower plenum at $t = 26s$.

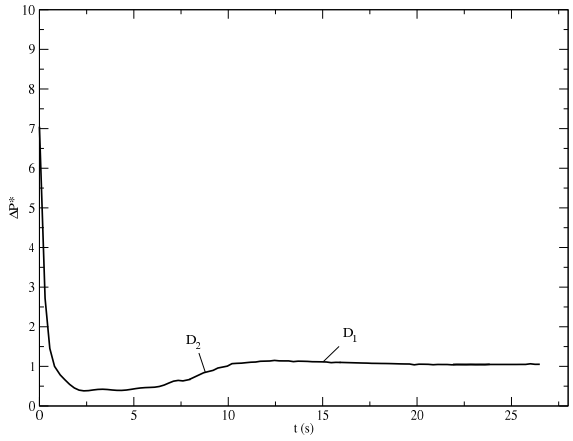

Figure 2.24: Test 1. Non dimensional pressure drop ΔP^* on D_1 and D_2 as a function of time.

pressure Δp^* initially at 7.3 drops to approximately 1.1. This implies that the pressure loss ΔP initially at $0.76bar$ drops to $0.12bar$. In this case we neglect the accidental pressure losses due to reactor grids.

In Figure 2.25 the temperature is shown over the plane at $z = 3m$ of the reactor at the point C_1 as a function of time. The point C_1 is at the center of the reactor.

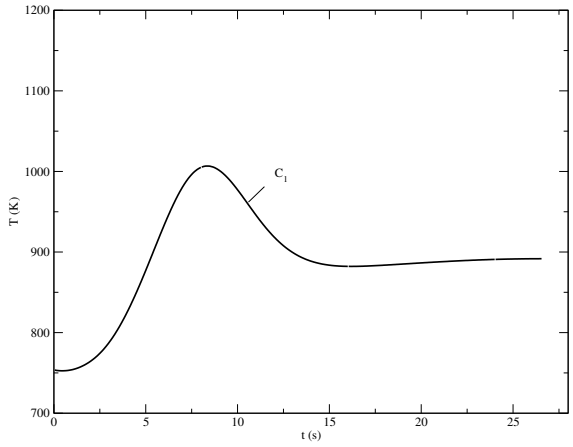

Figure 2.25: Test 1. The temperature profile at the point C_1 as a function of time.

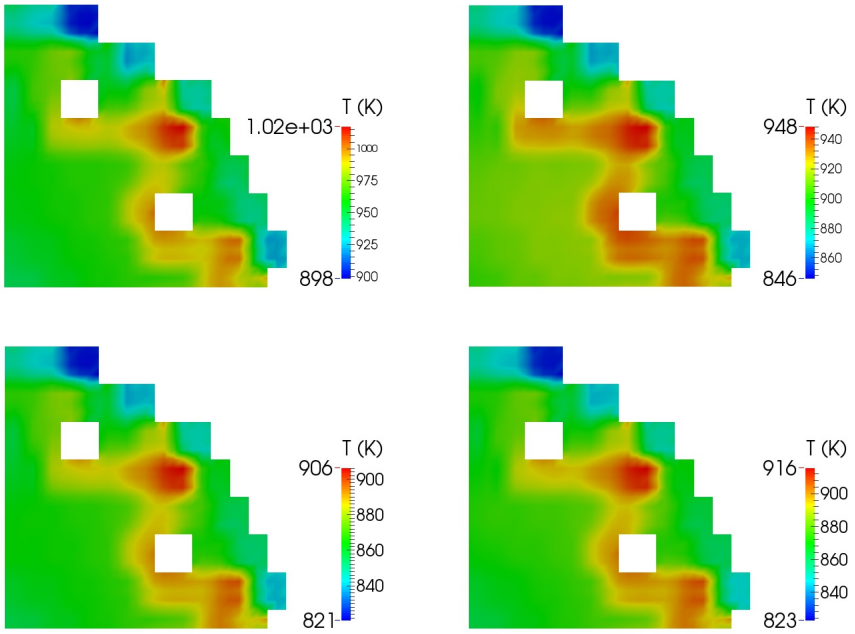

Figure 2.26: Test 1. Temperature profile on section at $z = 3.0m$ (defined by C_1, C_2, C_3, C_4) for $t = 8$, 10, 16 and 26 sec.

We note that in this point the temperature reach $1000K$ to come back to $900K$ after $15sec$. In Figure 2.26 one can see the temperature over the plane section at $z = 3.0m$ for $t = 8$, 10, 16 and 26 sec. In time there is a large initial temperature oscillation and then small fluctuations around an asymptotic distribution. The initial fluctuation leads to very high temperature above $1000K$ after approximately 8 sec. In Figure 2.26 it is easy to note that in all these oscillations the distribution of the fuel assembly defines the hot and cold spots of the reactor. At $t = 8$ more

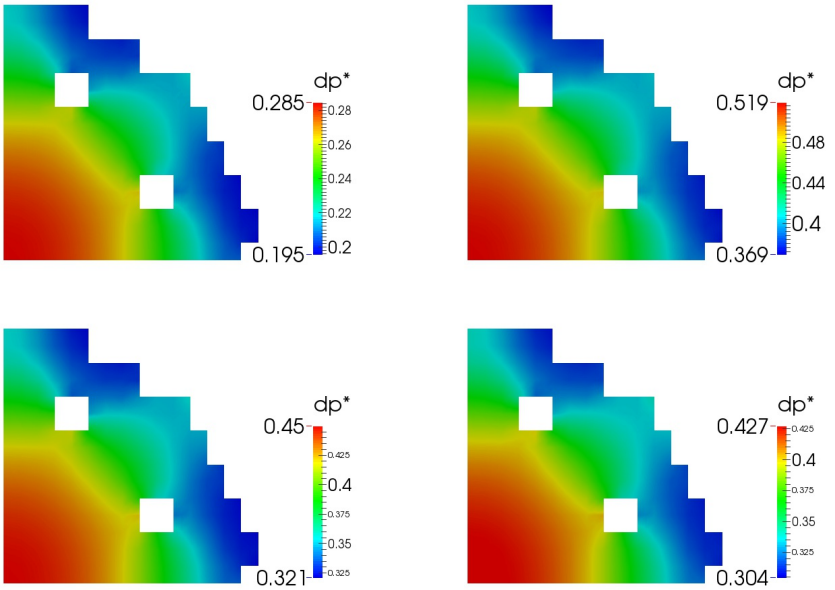

Figure 2.27: Test 1. Pressure profile on section at $z = 3.0m$ (defined by $C1, C2, C3, C4$) for $t = 8$, 10, 16 and 26 sec.

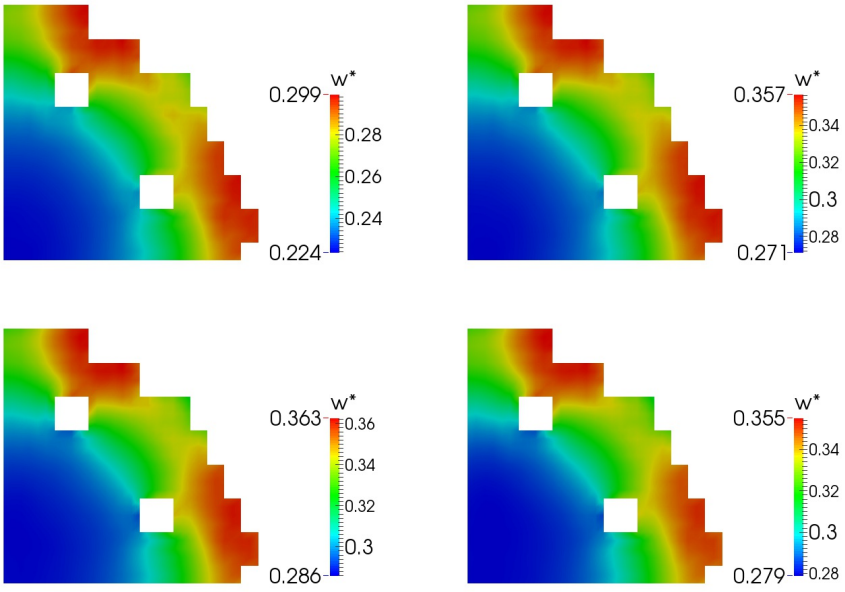

Figure 2.28: Test 1. Velocity profile on section at $z = 3.0m$ (defined by $C1, C2, C3, C4$) for $t = 8$, 10, 16 and 26 sec.

than hundred degree difference can be found between different regions. However at $t = 26s$ there is still a ninety degree difference between the hot and cold spots over

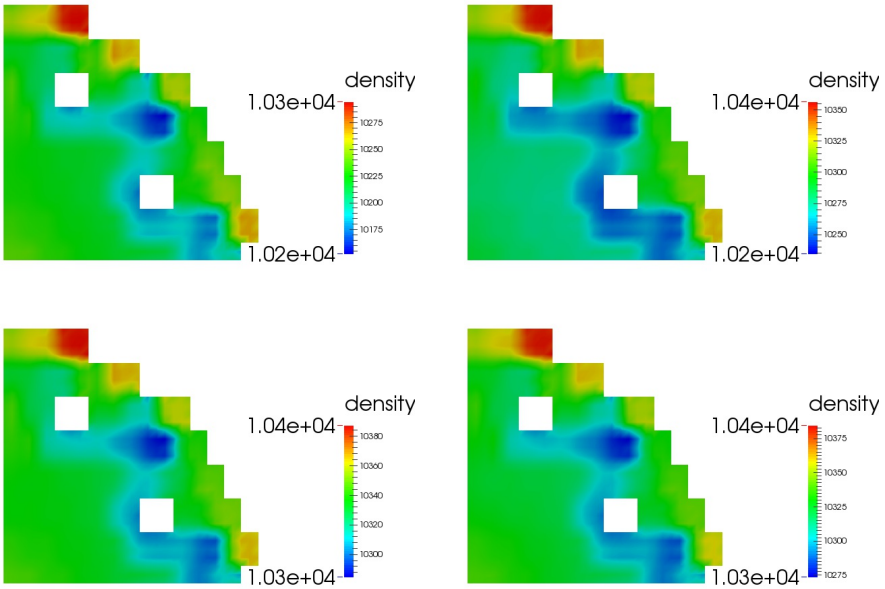

Figure 2.29: Test 1. Density profile on section at $z = 3.0m$ (defined by $C1, C2, C3, C4$) for $t = 8$, 10, 16 and 26 sec.

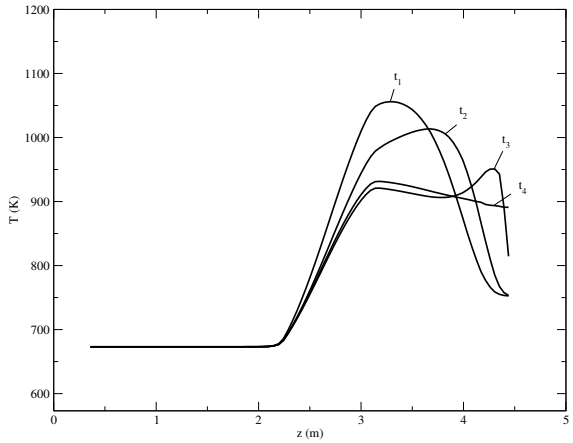

Figure 2.30: Test 1. Temperature profile on a vertical line passing through the point C_3 for $t = 8$ (t_1), 10 (t_2), 16 (t_3) and 26 (t_4) sec.

the section.

In Figures 2.27-2.28 the pressure and velocity distributions over the plane section at $z = 3.0m$ are shown for $t = 8$, 10, 16 and 26 sec. Large pressure variations imply the unstable nature of the natural convection flow. For each temperature distribution corresponds a distribution of density. The density profile on section at $z = 3.0m$ for $t = 8$, 10, 16 and 26 sec is shown in Figure 2.29.

In Figures 2.30 and 2.31 the temperature profile on a vertical line passing through

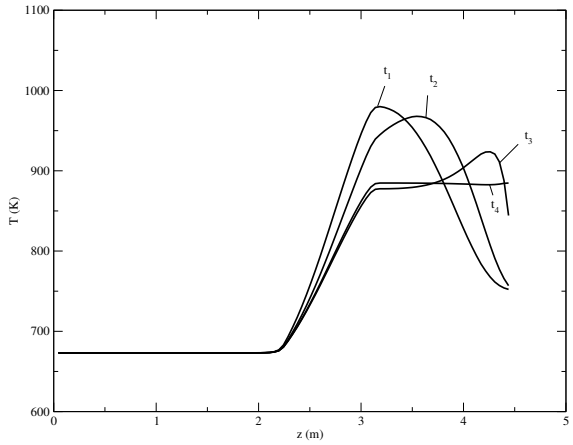

Figure 2.31: Test 1. Temperature profile on a vertical line passing through the point C_1 for $t = 8$ (t_1), 10 (t_2), 16 (t_3) and 26 (t_4) sec.

the point C_3 and C_1 are shown for $t = 8$ (t_1), 10 (t_2), 16 (t_3) and 26 (t_4) sec.

2.2.3 Primary loop evolution in natural convection flow

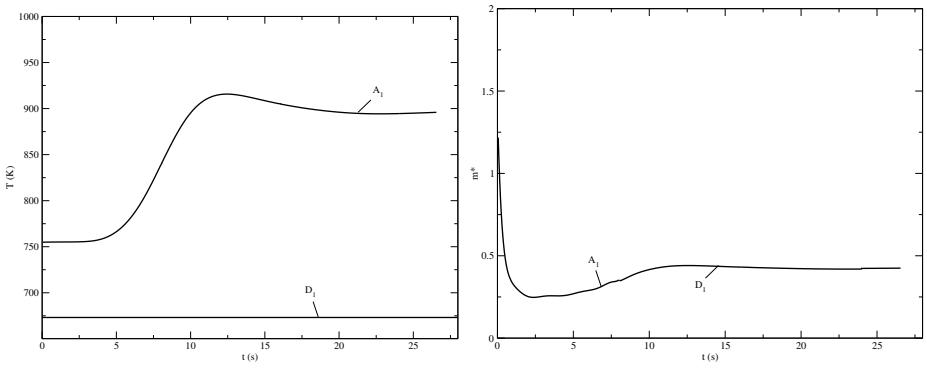

Figure 2.32: Test 1. Temperature (left) and non-dimensional mass $m^* = m/\rho_0 A$ (right) distribution in the primary loop A-D as a function of time.

In Figures 2.32-2.34 one can see the evolution of the primary loop witch is composed by two branches: A-D and B-D. The reactor is not completely symmetric and there are differences between the loop A-D and B-D. However the differences are very small and can be ignored according with the solutions shown in Figure 2.17 and Figure 2.18. In Figure 2.32 one can see the inlet and the outlet of the primary loop labeled A_1 (B_2) and D_1 (D_2) respectively. The mass fluxes from all the loops add up to the inlet of the lower plenum. In Figure 2.34 the pressure at the inlet and outlet of the primary loop is shown for the primary loop A-D on the left and B-D on the right. The pressure from the A-D loop defines the velocity in the left part of the plenum inlet while the pressure of the B-D loop defines the velocity in the right

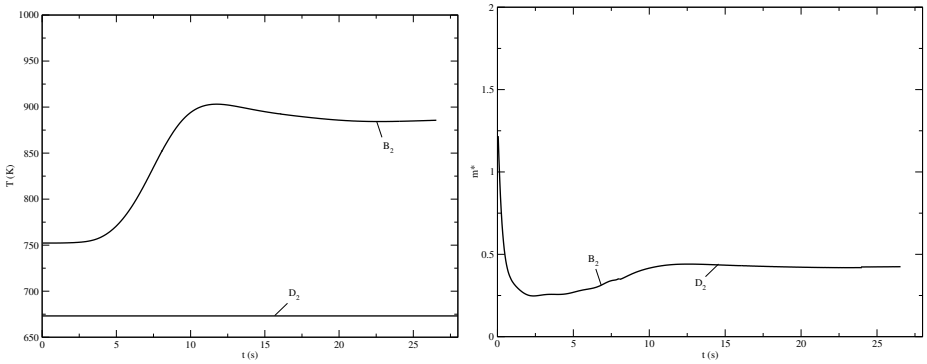

Figure 2.33: Test 1. Temperature (left) and non-dimensional mass $m^* = m/\rho_0 A$ (right) distribution in the primary loop B-D as a function of time.

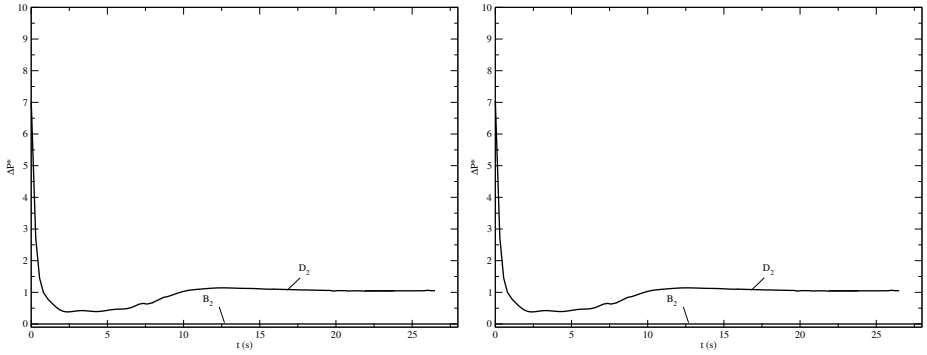

Figure 2.34: Test 1. Pressure distribution in the primary loop A-D (left) and B-D (right) at time $t = 0$.

one. If the pressure is the same on both branches then the inlet velocity is uniform. Otherwise greater is the pressure greater is the velocity in the corresponding area.

2.3 Test 2. Natural convection with 750MWth power

2.3.1 Initial conditions

The second test simulates the evolution of the system when the pumps are switched off and the heat source of the reactor is reduced of a 0.5 factor from its standard working conditions. This test allows us to evaluate the nature of the natural convection and the temperature that can be reached in the system. The reference point of this test is the same of the previous Section 2.2.1 and they are shown in Figure 2.11. In this Test 2 the initial conditions of the reactor is a steady solution in fully working condition with core average velocity of about $\bar{v} = 1.56m/s$. The corresponding average reduced velocity $\bar{v}^*$ is $\simeq 0.85$ with $r = 0.548$. The non-dimensional reduced mass flux $m^* = m/\rho_0 A$ in the left outlet of the upper plenum is 1.24886 and the corresponding mass flux of $m \simeq 16150Kg/s$ ($A \simeq 1.23m$ and $\rho_0 = 10563Kg/m^3$).

2.3.2 Reactor evolution in natural convection flow

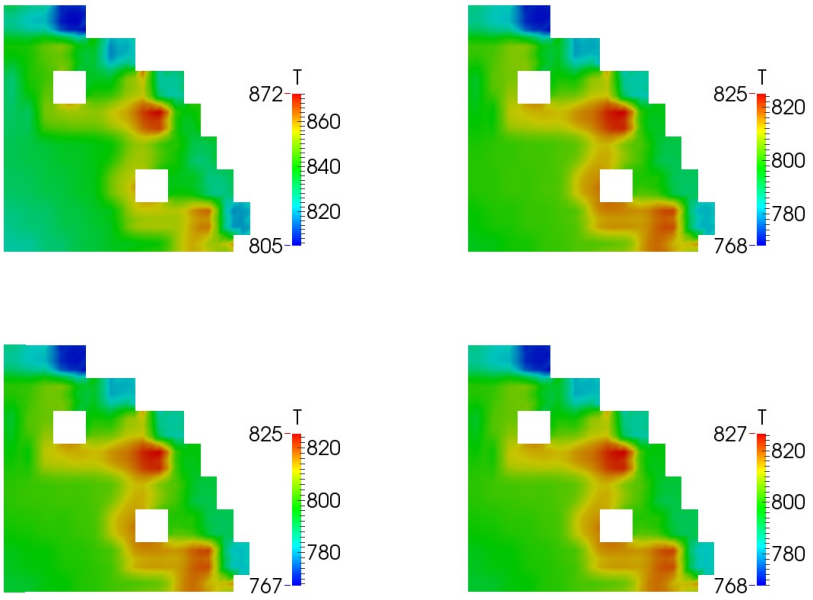

Figure 2.35: Test 2. Temperature profile on section at $z = 3.0m$ (defined by C_1, C_2, C_3, C_4) for $t = 8$, 16, 24 and 30 sec.

In Figure 2.35 one can see the temperature over the plane section at $z = 3.0m$ for $t = 8$, 10, 16 and 26 sec. In time there is a large initial temperature oscillation and then small fluctuations around an asymptotic distribution. The initial fluctuation

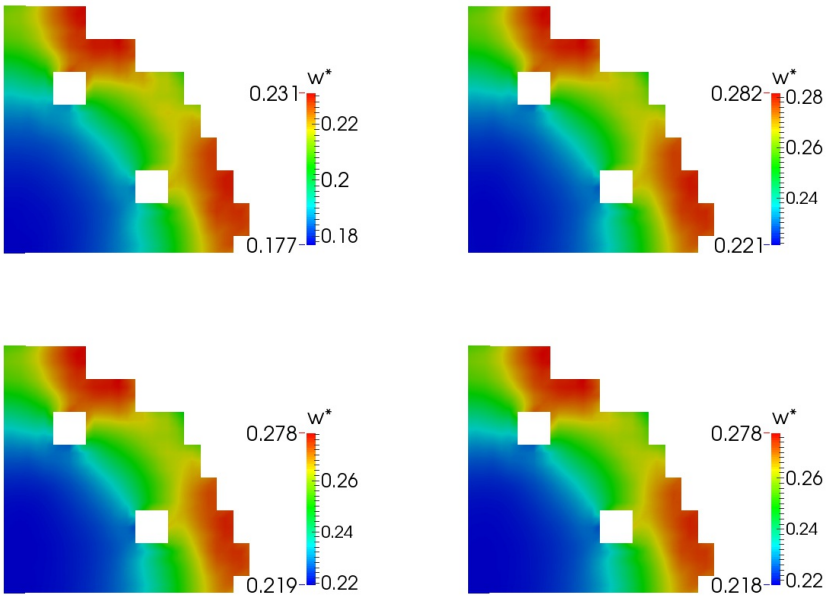

Figure 2.36: Test 2. Velocity profile on section at $z = 3.0m$ for $t = 8$, 16, 24 and 30 sec.

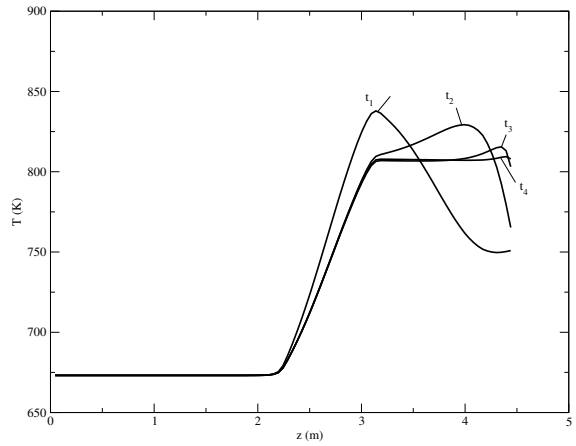

Figure 2.37: Test 2. Temperature profile on a vertical line passing through the point C_3 for $t = 8$ (t_1), 16 (t_2), 24 (t_3) and 30 (t_4) sec.

leads to a temperature not greater than $900K$ after approximately 8 sec. In Figure 2.35 it is easy to note that in all these oscillations the distribution of the fuel assembly defines the hot and cold spots of the reactor and leads to a difference between the zones of around seventy degrees which remains almost constant through time. In Figure 2.36 velocity distribution over the plane section at $z = 3.0m$ is shown at usual time step. We observe, first, an initial decrease of velocity and, then, a smooth

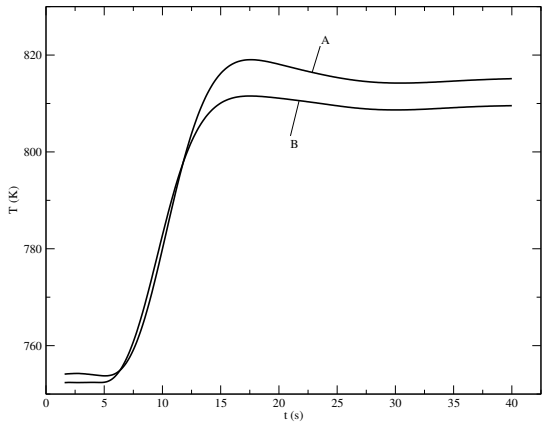

Figure 2.38: Test 2. Average temperature on left exit surface A and on the right exit surface B as a function of time.

increase which leads after ten seconds to the time independent value. In Figure 2.37 the temperature profile on a vertical line passing through the point C_3 is shown for $t = 8$ (t_1), 10 (t_2), 16 (t_3) and 26 (t_4) sec. We can notice that the initial decrease of velocity leads to a peak in temperature which does not overcome $850K$. In Figure 2.38 the outlet temperature on the two exits A, B is shown.

2.4 Test 3. Natural convection with 10MWth power (residual heat)

2.4.1 Initial conditions

The third test simulates the evolution of the system when the pumps are switched off and the heat source of the reactor is reduced of a 0.01 factor from its standard working conditions. The heat source imposed corresponds to the decay energy of the fission product and represent the minimal thermal power that have to be removed when the reactor is shuted down. This test allows us to evaluate if the natural convection in the reactor can remove such thermal power and evaluate the highest temperature reached in the core. In the Test 3 the initial conditions is a constant temperature in all the reactor of $608K$. The accidental pressure losses are neglected both in the reactor core and in the primary loop while the distributed pressure losses are considered.

2.4.2 Reactor evolution in natural convection flow

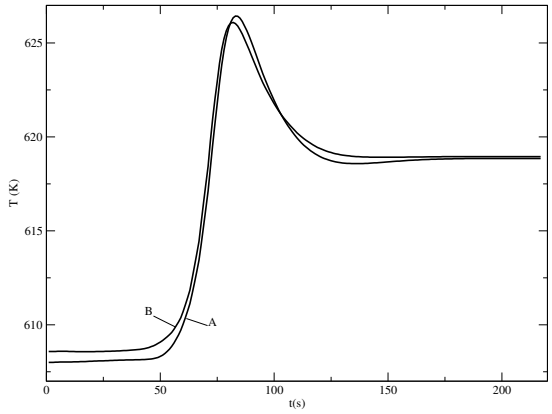

Figure 2.39: Test 3. Average temperature on left exit surface A and on the right exit surface B as a function of time.

During the time evolution the primary loop outlet is kept at constant temperature by the heat exchanger at temperature of $608K$. Both the primary loop A-D and B-D receive mass flux and temperature variable in time from the outlet surface A and B to return a flow with constant temperature. The reference temperature is $608K$ and the reference density $10641Kg/m^3$. In Figure 2.39 the outlet temperature on the two exits A, B is shown.

In Figure 2.40 one can see the temperature over the plane section at $z = 3.0m$ for $t = 8$, 40, 100 and 180 sec. In time there is a large initial temperature oscillation and the almost asymptotic distribution is reached after about 180 sec. The initial

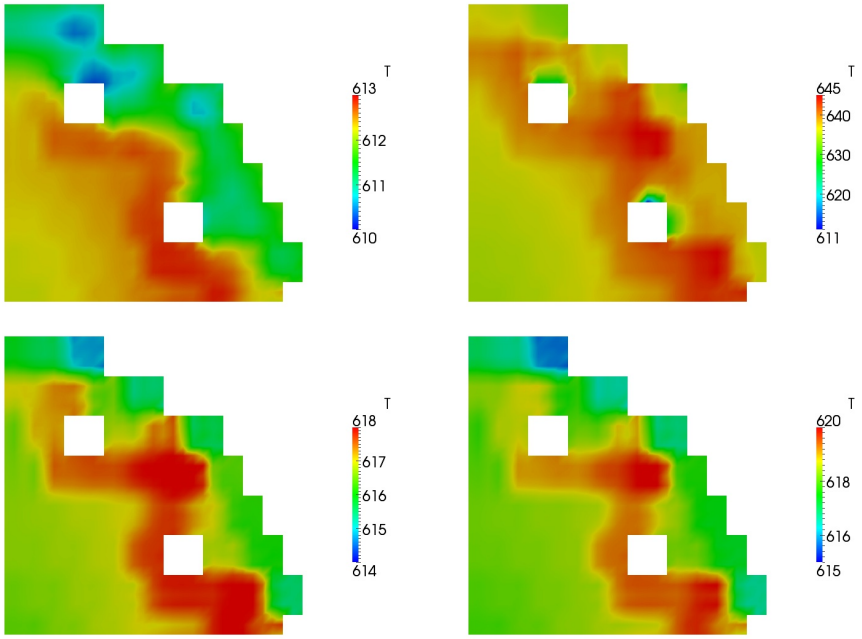

Figure 2.40: Test 3. Temperature profile on section at $z = 3.0m$ (defined by C_1, C_2, C_3, C_4) for $t = 8$, 40, 100 and 180 sec.

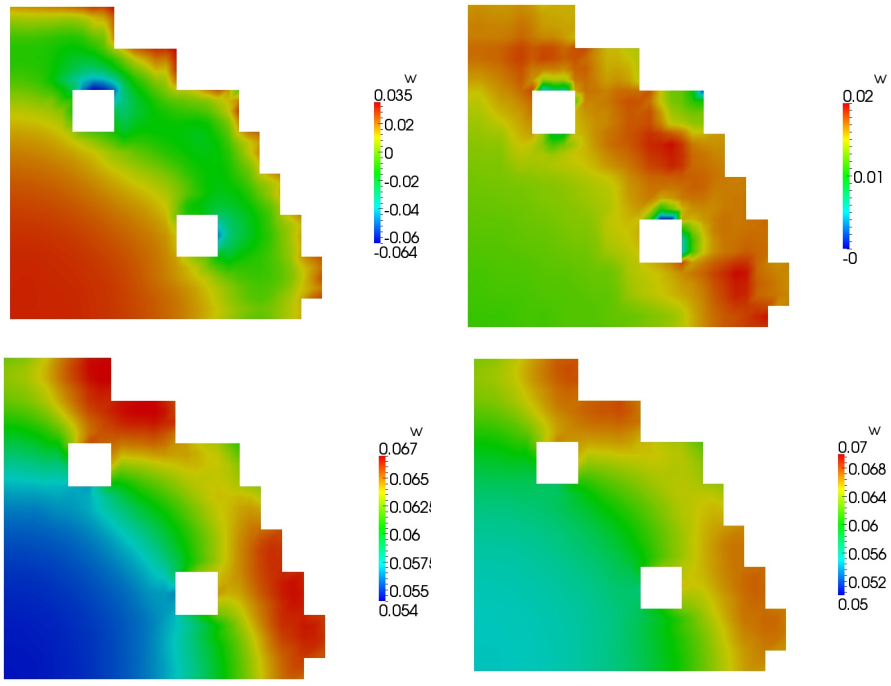

Figure 2.41: Test 3. Velocity profile on section at $z = 3.0m$ (defined by $C1, C2, C3, C4$) for $t = 8$, 40, 100 and 180 sec.

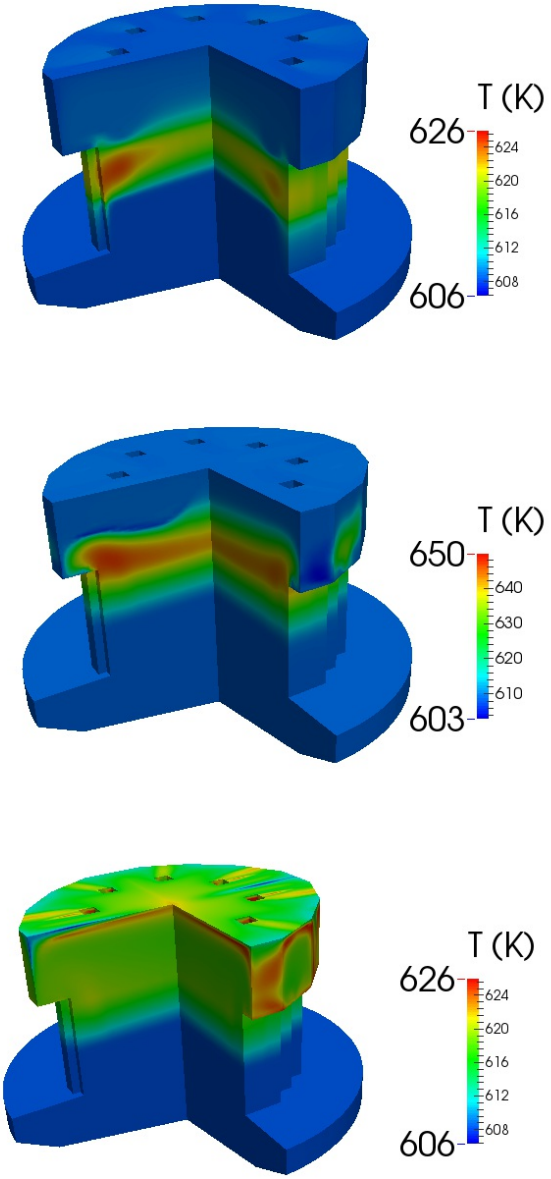

Figure 2.42: Test 3. Temperature distribution at $t = 0$, 50 and 100 sec.

fluctuation leads to a temperature not greater than $650K$ after approximately $40s$. This increase in temperature is due to the velocity reduction caused by the lack of the pump pressure. In Figure 2.40 it is easy to note that in all these oscillations the distribution of the fuel assembly defines the hot and cold spots of the reactor and leads to a difference between the zones of around thirty degrees at the beginning and a few degrees in the asymptotic solution. In Figure 2.41 velocity distributions over the plane section at $z = 3.0m$ are shown for different time steps. We observe

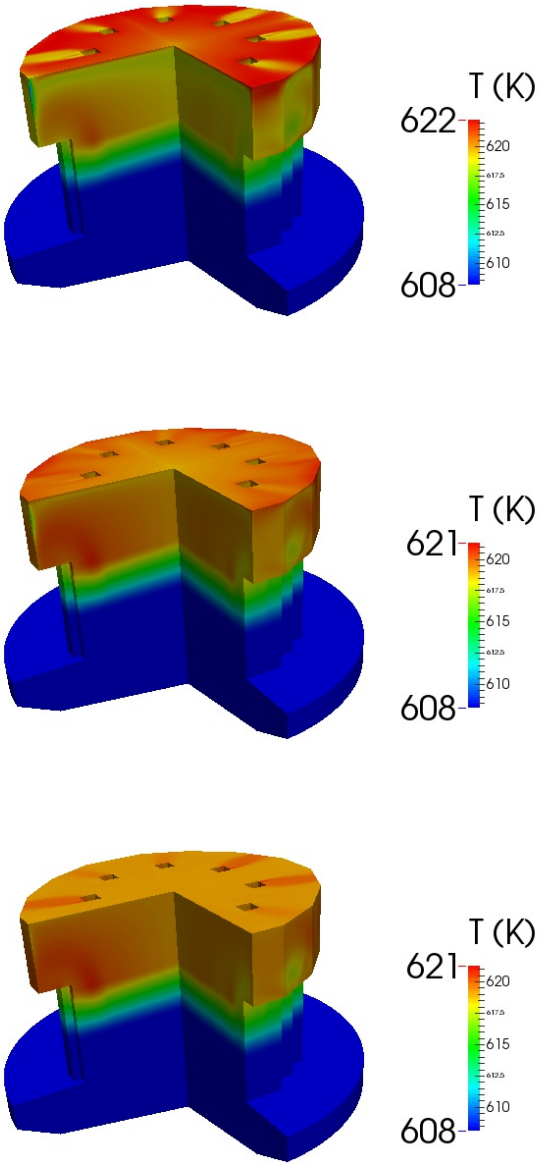

Figure 2.43: Test 3. Temperature distribution for $t = 130$, 150 and 200 sec.

an initial velocity decreasing but after ten seconds the velocity field tends to a small oscillatory behavior with almost time independent value. In Figures 2.42-2.43 one can see the evolution of the temperature distribution in the reactor. The temperature rises from the initial time to heat the top of the upper plenum at $t \simeq 100s$. After $180s$ the natural convection motion is established and the temperature distribution becomes a smoother solution.

In Figure 2.44 the temperature profile on a vertical line passing through the point

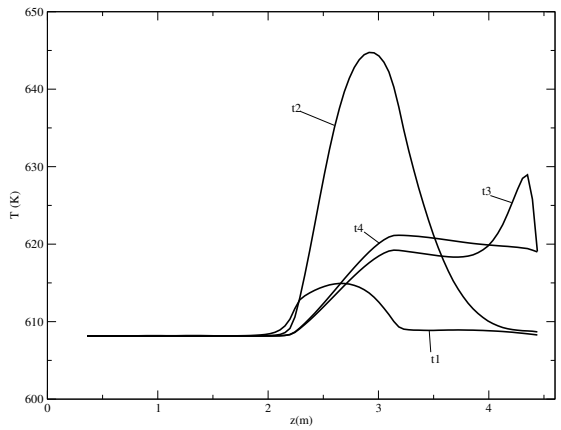

Figure 2.44: Test 3. Temperature profile on a vertical line passing through the point C_3 for $t = 8$ (t_1), 40 (t_2), 100 (t_3) and 180 (t_4) sec.

C_3 is shown for $t = 8$ (t_1), 40 (t_2), 100 (t_3) and 180 (t_4) sec. We can notice that the initial decreasing of velocity leads to a peak temperature which, hoverer, does not reach $650K$. The maximum temperature reached inside the core is relatively low but we remark that this is obtained with no accidental pressure losses in the steam generator. The accidental pressure losses in the inner/outer SG generator should not be too large to slow down significantly the flow inside the reactor in working conditions but they could become important in the free convection conditions with low flow rates. The removal of the heat decay could be done safely in natural convection regime. The maximum temperature in the core depends mainly on the design of the steam generator and its accidental pressure losses are the limiting factor of the natural convection flow rate.

Chapter 3

Numerical results: freezing model

3.1 Freezing model

In the design of LF reactors the coolant freezing in the pool may be considered one of the possible issue that may lead to a realistic accident. The simulation of three-dimensional phase changing from the liquid to the solid phase is very complex matter. However in order to investigate all possible problems related to this issue, a simple model has been proposed in [3]. This model is not a real two-phase model since the fluid remains in a single-phase even when the freezing occurs. The basic idea consists of approximating the freezing/melting process in a small temperature interval. This is not physically true since the freezing and melting are processes that transform kinetic energy into potential energy at constant temperature. However this temperature interval ΔT_m, called freezing temperature window, can be chosen arbitrary small. Inside this interval the temperature can define the phase of the system as

$$\gamma = \begin{cases} 0 & T \geq T_m \\ \frac{T - T_m}{\Delta T_m} & T_m - \Delta T_m \leq T \leq T_m \\ 1 & T \leq T_m - \Delta T_m \end{cases} . \tag{3.1}$$

In this way the temperature T, the freezing temperature T_m and the interval of freezing ΔT_m defines the state and phase of the system. For $T \leq T_m - \Delta T_m$ this system is solid, for $T \geq T_m$ the system is in liquid phase. For $T \in [T_m - \Delta T_m, \leq T_m]$ the system is changing the phase with the fraction of liquid set to γ.

The melting energy of the phase change can be taken into account by setting the specific heat C_p in the freezing interval ΔT_m. This implies to define the specific heat C_p as follows [3]

$$C_p = \begin{cases} 146.7 & T \geq T_m \\ 146700 & T_m - \Delta T_m \leq T \leq T_m \\ 146.7 & T \leq T_m - \Delta T_m \end{cases} . \tag{3.2}$$

The (3.2) implies that the enthalpy h of the system can be defined only from the

temperature. In fact for $\Delta T_m = 1.63$ the melting energy of phase change is

$$\Delta h_m = C_p \Delta T_m \approx 23800 J/kg\,. \tag{3.3}$$

With this choice the freezing temperature window ΔT_m can be computed in a physically consistent way where Δh_m becomes the heat released or absorbed by the system during the transforming process.

This model is a very convenient but it also may lead to large approximation. In fact this approximation neglects completely the space freezing physical aspects that are fundamental in two-phase flow. The freezing and melting are essentially surface phenomena. The freezing generally starts over an interface and propagates with the interface itself. The physics of the interface can be ignored in 0-dimensional or 1-dimensional problems but this may be important if not fundamental in three-dimension domains and low Reynolds numbers. However the three-dimensional two-phase flow with interface movement is extremely complex and as a first step to the study of the safety issue of a LFR one may consider the above approximation.

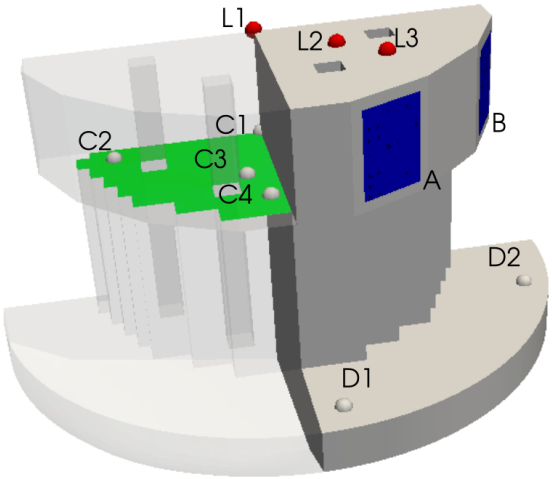

Figure 3.1: Test 4. Geometry for the freezing test.

In order to take into account the mechanical behavior of the fluid during the phase change and in the solid phase we introduce a force which simulates the growing resistance of the fluid during solidification. This is modeled by the use of pressure loss source terms in the momentum equation by setting the parameter β in the term

$$\mathbf{S} = \frac{1}{2}\beta_m \mathbf{v}|\mathbf{v}| \tag{3.4}$$

as

$$\beta_m = \begin{cases} 0 & T \geq T_m \\ 100\,\frac{T_m - T}{\Delta T_m} & T_m - \Delta T_m \leq T \leq T_m \\ 100 & T \leq T_m - \Delta T_m \end{cases} . \tag{3.5}$$

With the force introduced in (3.5) the flow slows down in the solid/fluid region due the strong increase of the force $\mathbf{S}$.

3.2 Test 4. Evolution of the freezing zone

3.2.1 Initial state

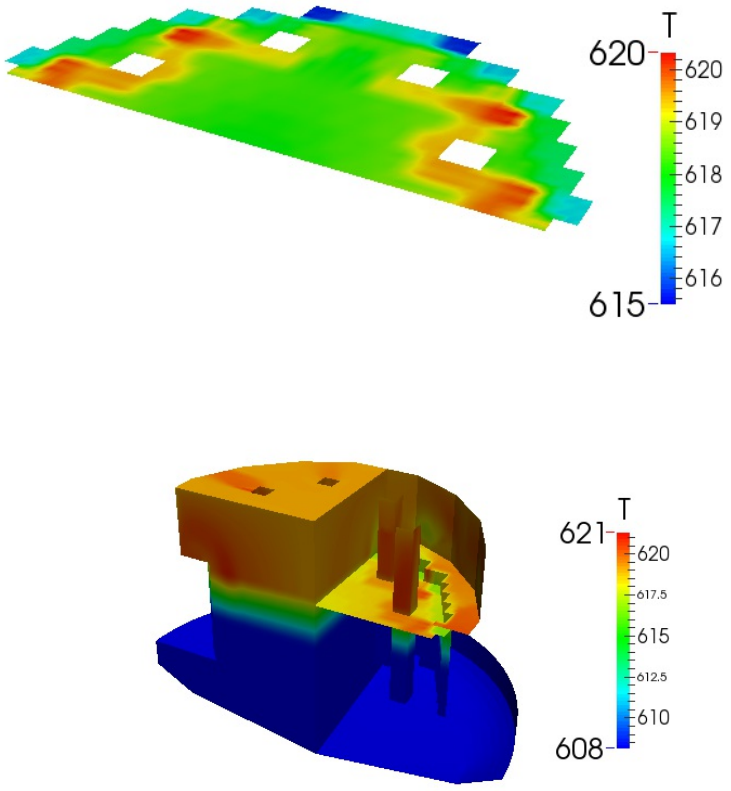

Figure 3.2: Test 4. Initial temperature distribution at $15MW$ and natural convection in the reactor and in the core outlet section ($z = 3.0m$).

In Test 4 we consider the usual geometry with the reference points as in Figure 3.1. Test 4 simulates the evolution of the system when the pumps are off and the heat source of the reactor is reduced to $15MWth$ in natural convection and a freezing accident occurs. In this test half the primary loop returns a mixture of solid/fluid lead with phase $\gamma = 0.4$. With the above model we have the inlet temperature $T = 599.485K$ over half of the reactor inlet and over the other half we have liquid lead at the temperature $T = 608K$. The initial configuration for this simulation. is the long time solution of the natural convection case with 15MWth power, inlet temperature $T = 608K$ and mass flow $8298.7Kg/m^2s$. In Figure 3.2 the temperature distribution at the initial time is shown in all the part of the reactor. The average temperature T_{in} over the inlet is $608K$ and average temperature in the

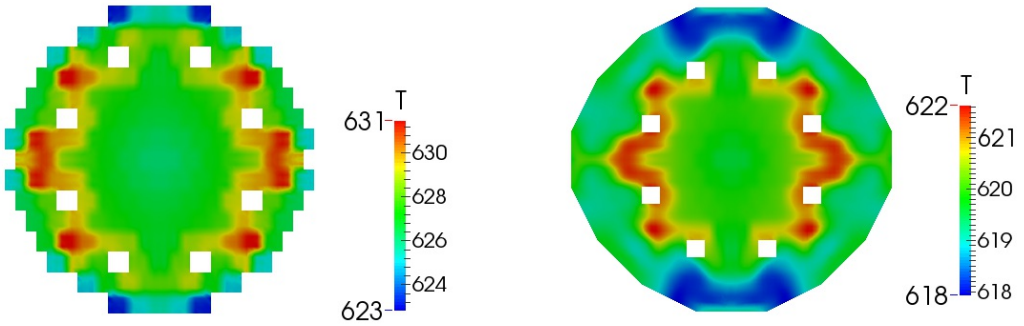

Figure 3.3: Test 1. Temperature distribution over the plane at $z = 3m$ (left) and $z = 3.5m$ (right) at time $t = 0$.

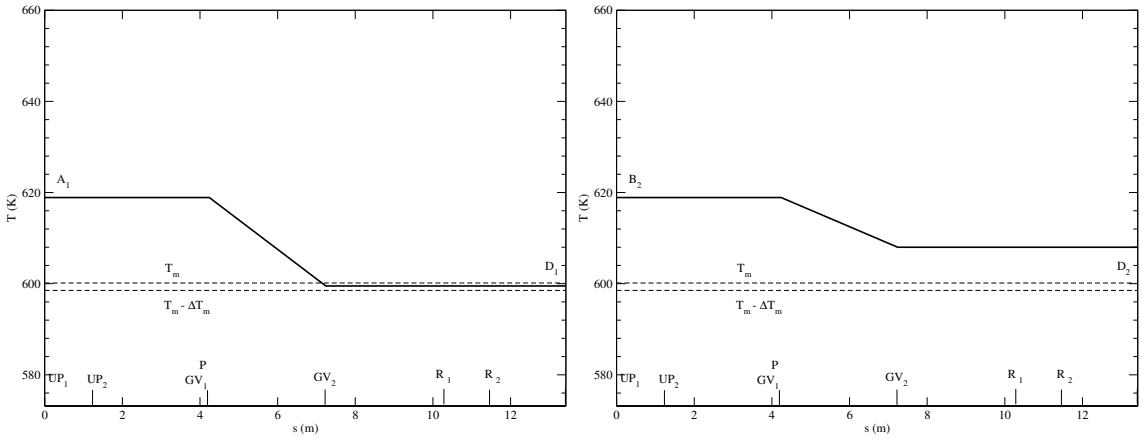

Figure 3.4: Test 4. Temperature along the 1D-p modules $A1$-$D1$ (right) and $B2$-$D2$ (left) at $t = 0$.

left and right outlet of the upper plenum is $619.2K$ for an inlet/outlet temperature difference of $11.2K$. In Figure 3.3 the initial temperature distribution over the plane at $z = 3m$ and $z = 3.5m$ are shown on the right and left, respectively. Over the plane at $z = 3m$ (core exit) the maximum temperature of this initial conditions is near the assembly with higher fuel peak factor. Over the plane obtained by a cut at $z = 3.5m$ the maximum temperature ($622K$) is in the region between the left and right exit of the upper plenum where a stagnation zone is located.

In Figures 3.4 temperature initial conditions are shown in the primary loop for the branch A-D and B-D on the right and left, respectively. The temperature is plotted as a function of the local mono-dimensional coordinate system. The GV_1 and GV_2 labels refer to the heat exchanger where the gravity is neglected. Initially the primary loop A-D gets fluid from the reactor at temperature $619.2K$ and returns to the reactor a mixture of solid/liquid material with phase set to 0.4.

3.2.2 Reactor evolution of the freezing zone

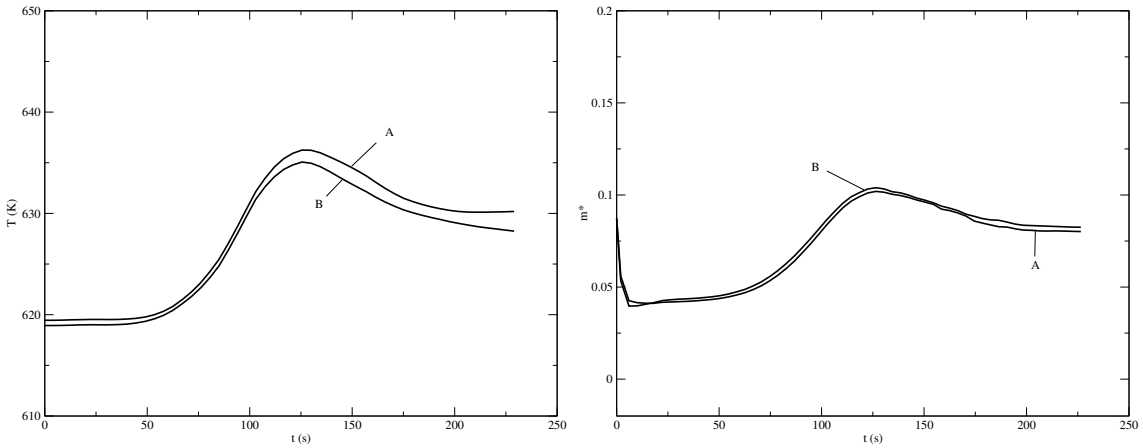

Figure 3.5: Test 4. Average temperature (right) and mass flux $m^* = m/\rho_0 A$ (right) on left exit surface A and on the right exit surface B as a function of time.

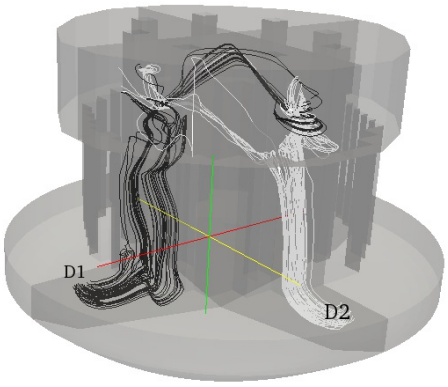

Figure 3.6: Test 4. Streamlines from D_1 and D_2.

The evolution of the freezing region at the melting point temperature can be evaluated by keeping the exit temperature of the primary loop A-D at the fixed value $T = 599.485K$, which is the temperature at the exit of the heat exchanger. At the given temperature $T = 599.485K$ the phase of the two-phase state of solid/liquid mixture is

$$\gamma = (600.15 - 599.485)/1.63 = 0.4\,. \tag{3.6}$$

This temperature over half the inlet is imposed as boundary condition. The other primary loop B-D is kept at temperature $608K$, which is slightly above the freezing temperature ($T_m = 600.15K$). With this boundary conditions we have a progressive cooling of the system since the energy that enters from the primary loop B-D is not

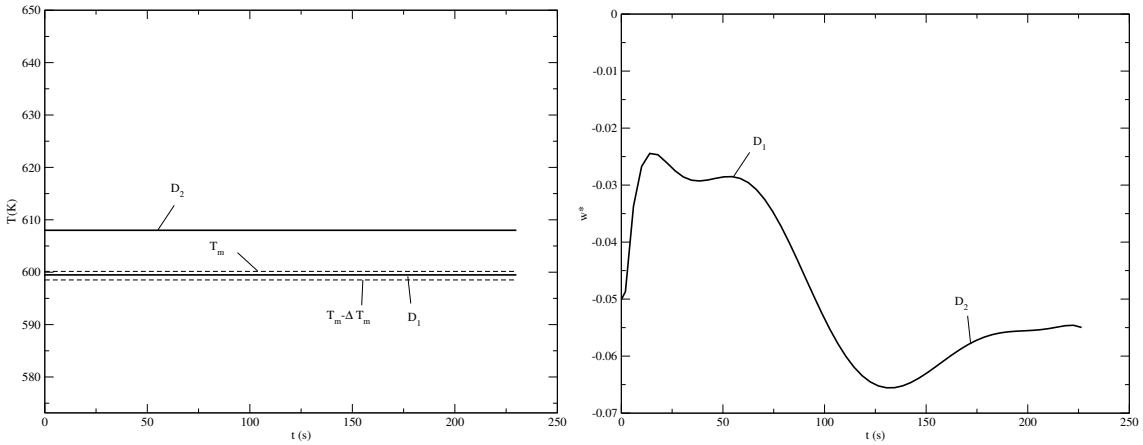

Figure 3.7: Test 4. Temperature (left) and velocity w^* (right) on D_1 and D_2 as a function of time.

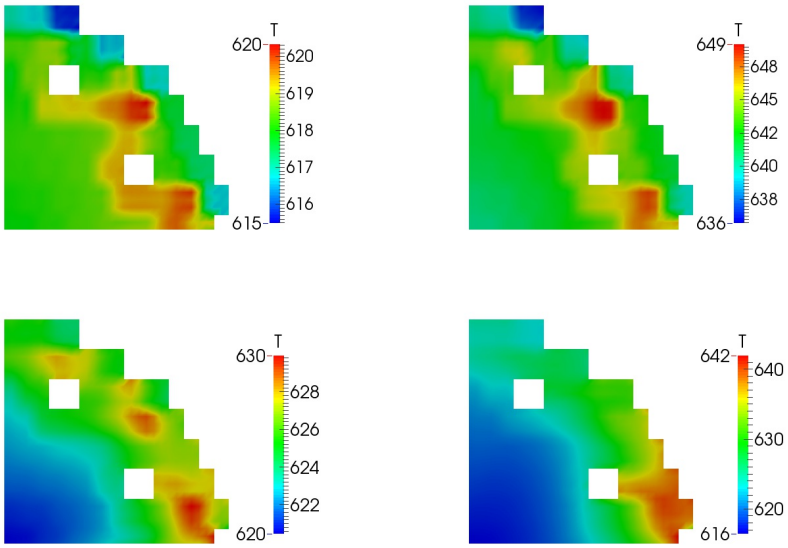

Figure 3.8: Test 4. Temperature distribution over the plane section at $z = 3.0m$ (core outlet) for $t = 0$, 50, 150 and $200s$.

sufficient to melt the solid/fluid mixture. Figure 3.5 shows the average temperature and the non-dimensional mass flux $m^* = m/\rho_0 A$ on left exit surface A and on the right exit surface B as a function of time. At first the average temperature increases since the resistance of the fluid slows down the motion. But soon the increasing of the temperature improves the natural convection with the corresponding cooling. From Figure 3.5 one can see that the exit average temperature is higher in the exit A where the freezing mixture is introduced. This effect is due to the flow path and the different flow resistance of the mixture with respect to the single fluid phase. In

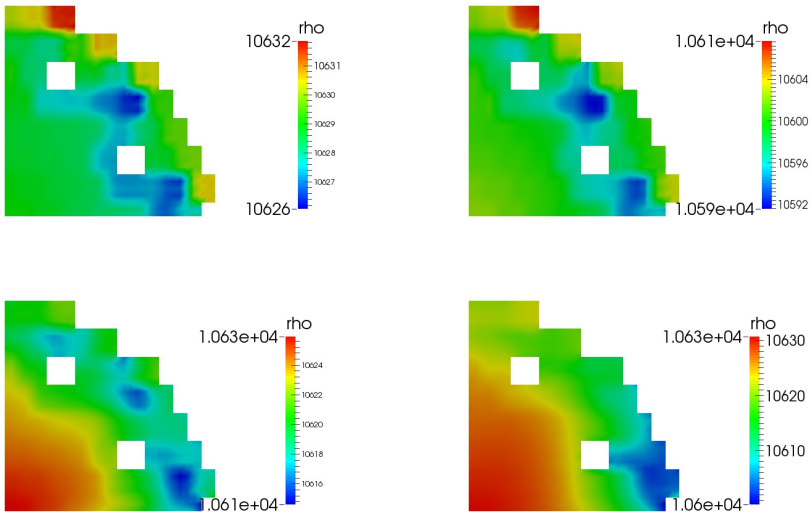

Figure 3.9: Test 4. Density distribution over the plane section at $z = 3.0m$ (core outlet) for $t = 0$, 50, 150 and $200s$.

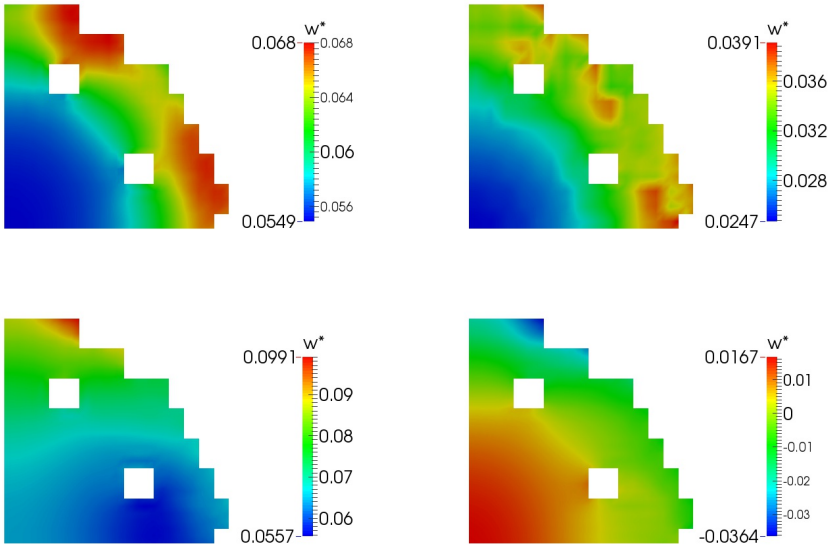

Figure 3.10: Test 4. Reduced w-component of the velocity $\mathbf{v}*$ distribution over the plane section at $z = 3.0m$ (core outlet) for $t = 0$, 50, 150 and $200s$.

Figure 3.6 streamlines from D_1 and D_2 are reported at $t = 200s$. These streamlines show that the flow path prefers the exit B in the primary branch B-D for the simple reason that more viscous forces are present where the the solid phase γ increases. In Figure 3.7 one can see temperature and reduced velocity w^* (right) at the points

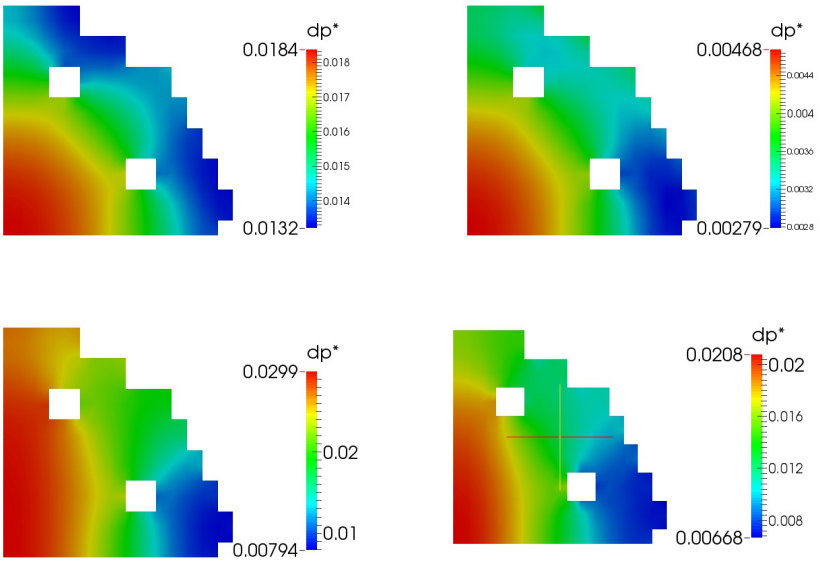

Figure 3.11: Test 4. Pressure distribution over the plane section at $z = 3.0m$ (core outlet) for $t = 0$, 50, 150 and $200s$.

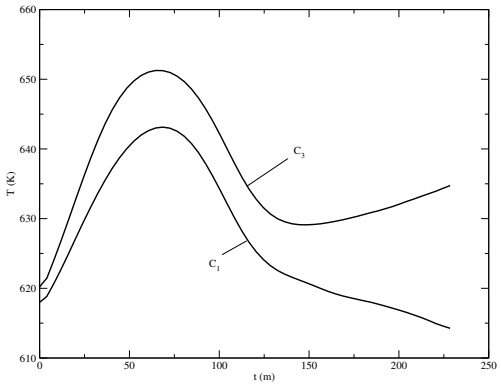

Figure 3.12: Test 4. Temperature profile on the core outlet surface at the point $C1$ and $C3$ as a function of time.

D_1 and D_2 of the lower plenum inlet as a function of time. Over these points we impose the boundary conditions with pressure and temperature taken by the two branches of the primary loops. In Figure 3.8-3.11 temperature, density velocity and pressure distributions over the plane section at $z = 3.0m$, near the core outlet, for $t = 0$, 50, 150 and $200s$ are shown. Finally on this surface the temperature profile at the point C_1 and C_3 are reported as a function of time in Figure 3.12.

During the evolution the freezing region from the lower plenum inlet progresses to the core. In Figure 3.13 the evolution of the freezing region is shown for $t = 0$,$t = 50$, 100, 150 and $200s$. The plane section at $z = 1.0m$ is just right below the core inlet

Figure 3.13: Test 4. Evolution of the freezing region for $t = 0$,$t = 50$, 100, 150 and $200s$.

and over this plane, as shown in Figure 3.14 the temperature decreases in time In this figure we can see the temperature evolution for $t = 0$, 50, 150 and $200s$. The plane at $z = 1.0m$ cuts the lower plenum inlet and the liquid/solid zone progressively expands from the inlet region to the interior of the domain.

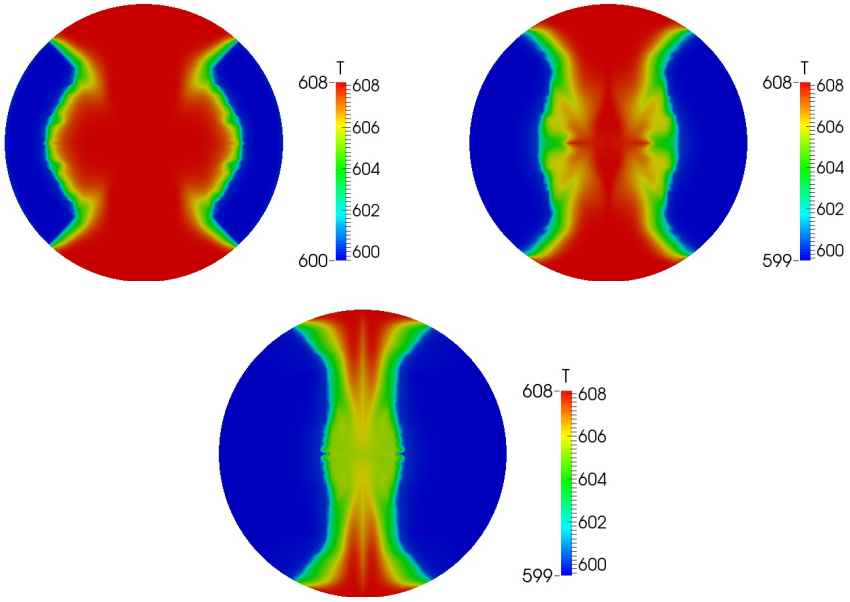

Figure 3.14: Test 4. Temperature distribution over the plane section at $z = 1.0m$ (core outlet) for $t = 0$, 50, 150 and $200s$.

3.2.3 Primary loop evolution

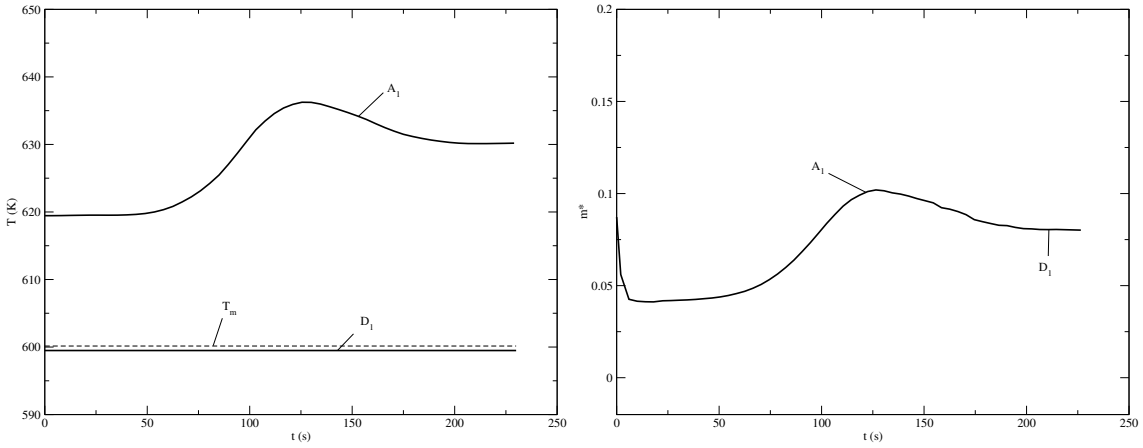

Figure 3.15: Test 4. Temperature (left) and velocity w^* (right) on $A_1$and D_1 as a function of time.

In Figures 3.15-3.16 one can see the evolution of the primary loop which consists of two different branches: A-D and B-D. The schematic representation of a primary loop circuit is reported in the previous section in Figure 2.6. The fluid goes from the upper plenum through the heat exchanger to the lower plenum. The upper plenum height is $1.24m$ and the heat exchanger is evaluated to be located $3m$ above. These

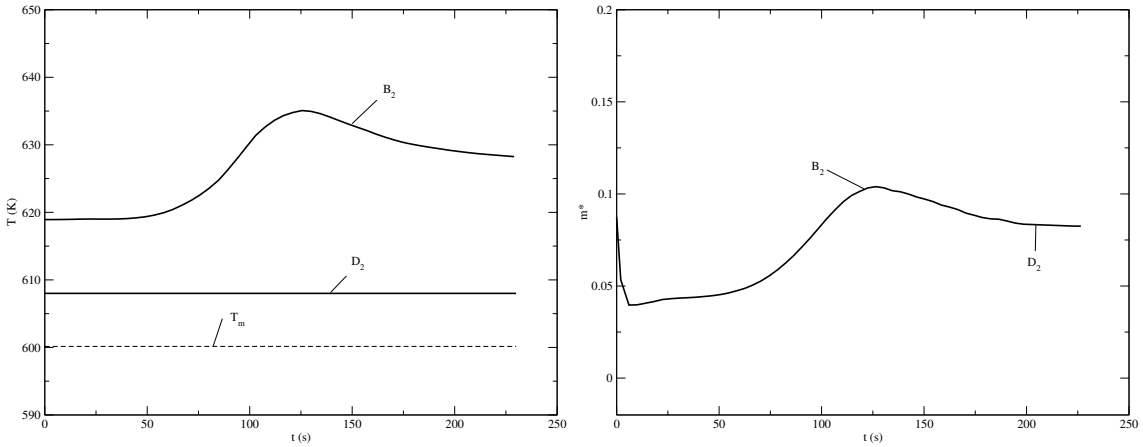

Figure 3.16: Test 4. Temperature (left) and velocity w^* (right) on $D_1$and D_2 as a function of time.

heights drive the natural convection in the primary loop which has the pump off. The primary loop A_1-D_1 receives liquid lead at variable time dependent temperature from the reactor which, after going through the heat exchanger, become partially solid. The primary loop A_1-D_1 pours into the reactor the liquid/solid mixture at fixed temperature and phase. The temperature and non-dimensional mass $m^* = m/\rho_0 A$ distribution in the primary loop A-D as a function of time are shown in Figure 3.15. The primary loop B_2-D_2 receives from the reactor liquid lead at variable time dependent temperature which, after going through the heat exchanger, reaches the fixed temperature $T = 608K$. The temperature and non-dimensional mass m^* distribution in the primary loop B-D as a function of time is shown in Figure 3.16. Since the reference inlet temperature is $608K$ the reference density ρ_0 is $10641kg/m^3$.

3.3 Test 5. Evolution of the melting zone

The model, described in Section 3, is valid for freezing processes but it is also valid when melting occurs. By starting from a previous configuration of the Test 4 we increase the reactor power to induce melting of the solid/fluid mixture into single phase fluid.

3.3.1 Initial state

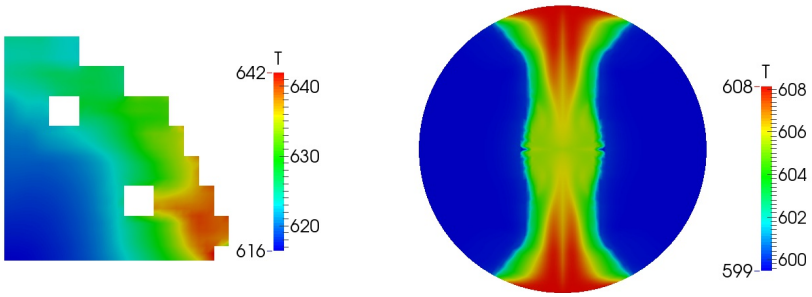

Figure 3.17: Test 5. Initial temperature distribution over the inlet surface (right) and at $z = 3m$ (on left).

In Test 5 we consider the usual geometry as in Figure 3.1 and simulate the evolution of the system when the pumps are off and the heat source of the reactor increases from 15MWth to $150MW$th. The boundary conditions are the same as Test 4 The primary loop, in the branch A-D, returns a mixture of solid/fluid lead with phase $\gamma = 0.4$ at melting point temperature ($599.485K$). The other half of the primary loop pours liquid lead at the corresponding outlet temperature. In order to increase the inlet temperature needed to melt the mixture into single fluid we suppose that the lead is not cooled in this primary branch of the primary loop. The long time solution of the previous natural convection case with 15MWth power, reported in Test 4, is taken as initial condition. In Figure 3.17 the initial temperature distribution is shown over the inlet plane on the right, and over the plane at $z = 3m$ (core exit) on the left. The maximum temperature of this initial conditions is reached near the exit above the two-phase mixture because of the lower intensity of the velocity field. Initially the primary loop A-D gets fluid from the reactor at temperature about $625K$ and returns to the reactor a mixture of solid/liquid material with phase 0.4 while the other primary loop B-D gets fluid from the reactor at temperature about $630K$ and returns to the reactor fluid lead at the same value because we suppose the by-pass of the heat exchanger.

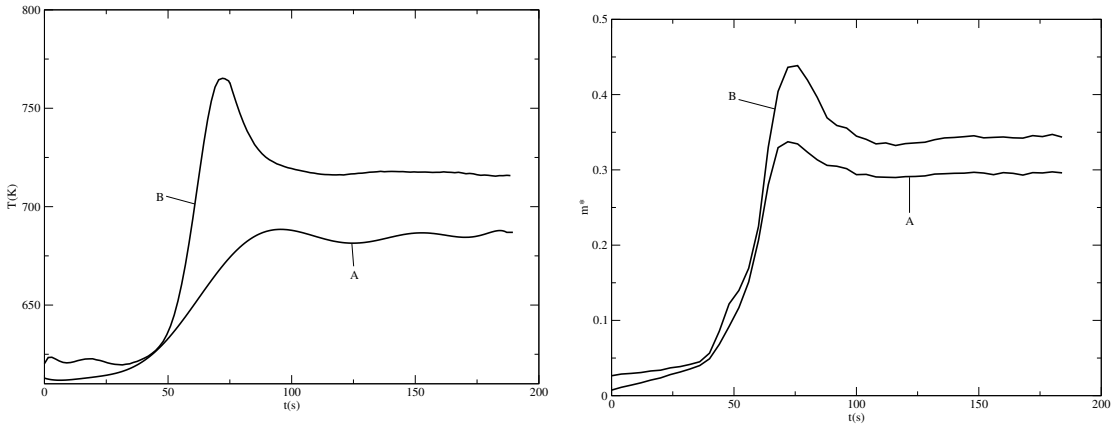

Figure 3.18: Test 5. Average temperature (right) and mass flux $m^* = m/\rho_0 A$ (right) on left exit surface A and on the right exit surface B as a function of time.

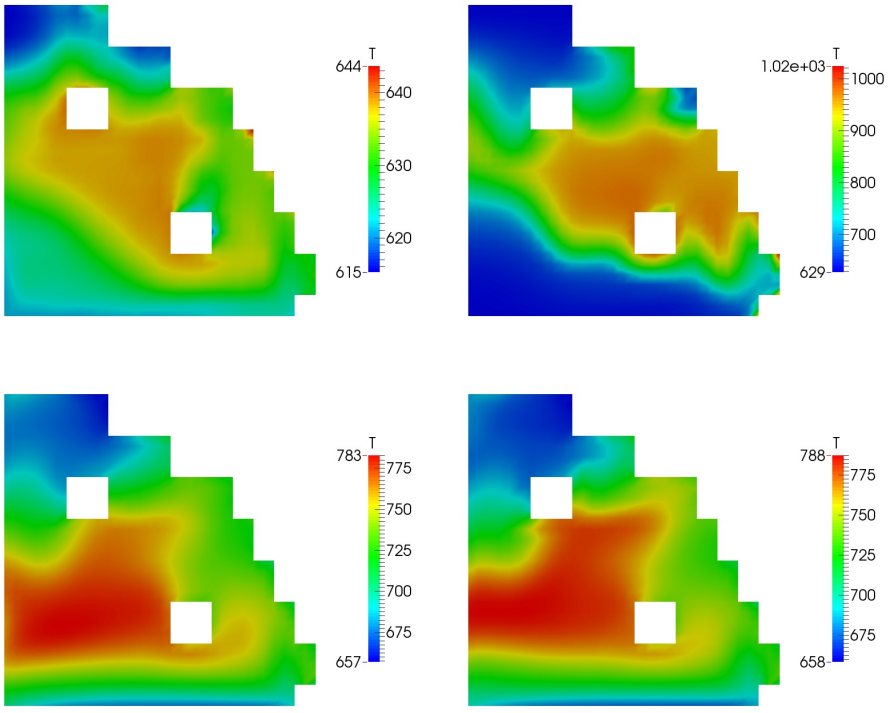

Figure 3.19: Test 5. Temperature distribution over the plane section at $z = 3.0m$ (core outlet) for $t = 0$, 50, 150 and $200s$.

3.3.2 Reactor evolution of the melting zone

The evolution of the freezing region at the melting point temperature can be evaluated by keeping the exit temperature of the primary loop A-D at the fixed value

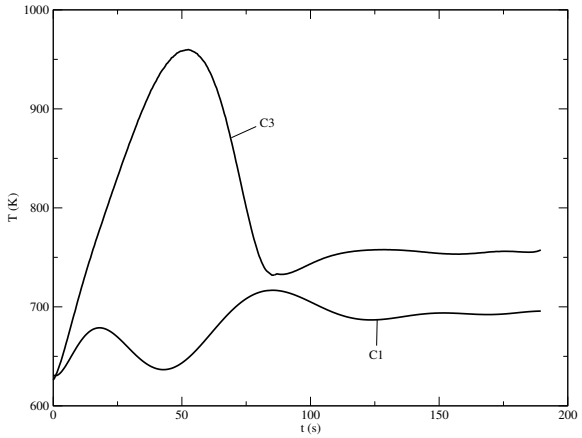

Figure 3.20: Test 5. Temperature profile on the core outlet surface at the point C_1 and C_3 as a function of time.

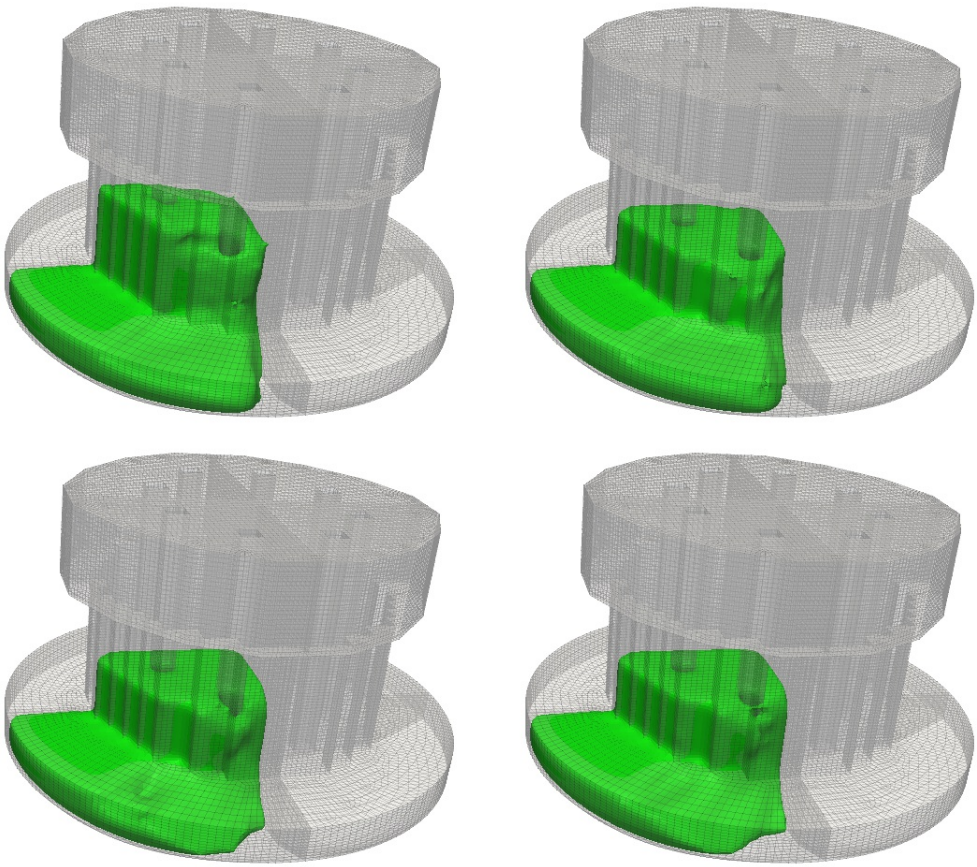

Figure 3.21: Test 5. Evolution of the freezing region for $t = 0$, 50, 100 and $150s$.

$T = 599.485K$, which is the temperature at the exit of the heat exchanger. We

imposed this temperature over half inlet in the lower plenum. The other primary loop B-D is kept at constant temperature whose value depends on the average temperature on the B section that increases in time together with the heat core source. With this boundary conditions we have a progressive melting of the liquid/solid mixture already present in the system. Figure 3.18 shows the average temperature and the non-dimensional mass flux m^* on left exit surface A and on the right exit surface B as a function of time. Initially the average temperature increases since the resistance of the fluid slows down the motion. When the velocity field grows up we observe a decrease of the temperature field. At the end of the time interval monitored in the simulation we notice a difference between the average temperature of the exits of about $90K$. In Figure 3.19 temperature over the plane section at $z = 3.0m$, near the core outlet, for $t = 0$, 50, 150 and $200s$ are shown. Over this plane in Figure 3.20 the temperature profile on the core outlet surface at the point C_1 and C_3 are reported as a function of time.

During the evolution the melting region from the lower plenum inlet progresses to the core. In Figure 3.21 the evolution of the freezing region is shown for $t = 0$, 50, 100, 150 and $200s$. As one can see from Figure 3.21 the region, colored in green, with solid/liquid mixture shrinks. The region close to the core inlet levels towards the bottom and the channel with liquid coolant enlarges on the right side of the lower plenum inlet. The decreasing of the region with two-phase flow is slow but steady.

3.3.3 Primary loop evolution

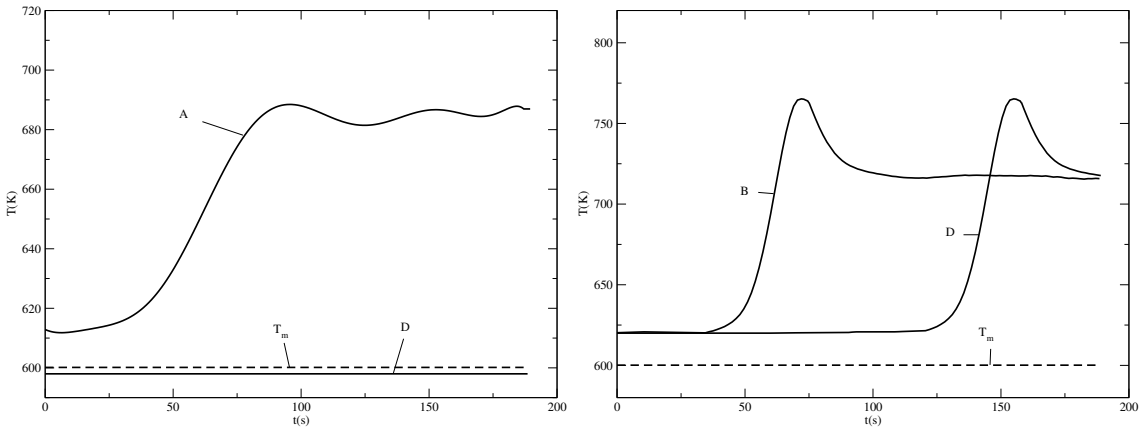

Figure 3.22: Test 5. Temperature as a function of time on A-D (left) on B-D (right).

In Figure 3.22 one can see the evolution of the two different branches of the primary loop. The schematic representation of a primary loop circuit is reported in the previous section in Figure 2.6. The fluid goes from the upper plenum through the heat exchanger to the lower plenum. The primary loop A-D receives liquid lead

at variable time dependent temperature from the reactor which, after going through the heat exchanger, becomes a mixture of solid and liquid material. The primary loop A-D pours into the reactor this mixture at fixed temperature and phase.

In the primary loop the pumps are off and only natural convection drives the flow. The primary loop B-D receives from the reactor liquid lead at variable time dependent temperature. This flow temperature remains constant along the primary loop path because we suppose a by-pass circuit of the heat exchanger. So, as we can see in Figure 3.22, the temporal evolution of the temperature in B and D are equal but shifted over the interval time needed by the coolant to go from B to D.

Conclusions

In this report we presented the development of the FEM-LCORE code for studying LFR three-dimensional thermohydraulics. The current version of the FEM-LCORE code can analyze transient phenomena and allow the investigation of freezing events and, moreover, study the natural convection flow in the reactor. We have tested this version with different thermal power levels and working conditions. The test in natural convection shows that the decaying heat can be removed easily if the accidental pressure losses of the core grids and steam generator are neglected. From this the design of the steam generator and its accidental pressure losses become the key factor of the natural convection flow rate. From all presented tests, we can summarize that the code may be easily used to study a large range of different LFR reactors but further improvement and validation should be carried out. The physical model of freezing phenomena must be improved together with the heat removal model used to simulate the steam generation in the primary loop. The reactor primary circuit, the plenum and the core may be investigated at three different scale levels even if the standard approach is to study the reactor with 3D-CFD tools and the rest of the primary circuit with mono-dimensional system codes. The coupling between the core and the plenum can be studied with the current FEM-LCORE code but the interface with the rest of the primary loop is still under investigation. A further improvement in this direction might be the coupling between FEM-LCORE and a system code, like CATHARE, to simulate the entire primary loop inside the SALOME platform but at the moment the CATHARE-SALOME and FEM-LCORE-SALOME integration modules are still under development.

Bibliography

[1] *ELSY Work Program. European Lead-cooled SYstem (ELSY) Project*, Technical report, EURATOM, Management of Radioactive Waste (2006). 20, 35

[2] L. Cinotti, "Reactor Assembly preliminary Configuration", ELSY DOC 08 049, Del Fungo Giera Energia, (2008). 32

[3] I. Di Piazza, *Freezing of the LFR primary pool: CFD modeling and preliminary analysis on prototypical configuration* Technical report ENEA (2012). 59

[4] A. Alemberti, J. Carlsson, E. Malambu, A. Orden, D. Struwe, P. Agostini, S. Monti, *European lead fast reactor—ELSY*, Nucl. Eng. Design, 241, pp.3470-3480 (2011). 32, 35

[5] X. Cheng, N.I. Tak, *CFD analysis of thermal-hydraulic behavior of heavy liquid metals in sub-channels*, Nucl. Eng. Design, 236, pp.1874-1885 (2006). 22

[6] I. Di Piazza, M. Scarpa, *Rassegna di Letteratura sulla Termoidraulica dei Bundle Refrigerati a Metallo Liquido Pesante*, ENEA Report LM-FR-001 (2012). 37

[7] A. Cervone and S. Manservisi, *A three-dimensional CFD program for the simulation of the thermo-hydraulic behavior of an open core liquid metal reactor*, Technical report lin-thrg 108-2008. 11, 13, 14, 16, 17, 24

[8] S. Bnà, S. Manservisi and O. Le Bot, *Simulation of the Thermal-hydraulic behavior of Liquid Metal Reactors using a Three-Dimensional Finite Element Model*, Technical Report DIENCA-UNIBO 2010. 10, 11, 13, 14, 16, 17, 24, 33

[9] F. G. Bornia, M. Finelli, S. Manservisi, V. Mikhin, M. Polidori and K. Voukelatou, *Development and validation of FEM-LCORE code for the thermal hydraulics of open cores*, Technical Report DIENCA-UNIBO 2011. 10, 11, 17, 24

[10] G. Bornia, D. Cerroni, S. Manservisi, M. Polidori and F. Donato, *FEM-LCORE code: parallelization, turbulence models and code integration*, Technical Report ENEA-UNIBO 2012. 9, 10, 11, 17

[11] F.Bassenghi, G.Bornia, L.Deon and S. Manservisi, *Implementation and validation of the NURISP platform*, Technical report CIRTEN-UNIBO 2011. 10

[12] F.Bassenghi, G.Bornia, A. Cervone and S. Manservisi, *The ENEA-CRESCO platform for simulating liquid metal reactor*, Technical report LIN-THRG 210-2010. 10

[13] L. Barucca, M. Gregorini, *DHR Main components Functional Sizing*, DOC/08/047, Ansaldo Nucleare, (2008). 38

[14] M. Bottcher, *CFX Analyses of the RVACS Decay Heat Removal System*, KIT/INR-09-01, Wissenschaftliche Berichte (2009). 38

[15] L. Cinotti, *Reactor Assembly preliminary Configuration*, ELSY-DOC08049, Del Fungo Giera Energia (2008). 20, 35

[16] A. Onea, M. Bottcher, D. Struwe, *Analysis of the pressure loss through the heat exchanger for the primary side of the ELSY nuclear reactor*, KIT/INR-09-03, Wissenschaftliche Berichte (2009). 38

[17] A. Onea, M. Bottcher, D. Struwe, *Detailed CFD analysis of the pressure loss on the primary side for the heat exchanger of the ELSY fast lead-cooled reactor by applying unit slice models*, ASME-ATI-UIT, Sorrento, Italy (2010). 38

[18] A.Travleev, *ELSY core design static, dynamic and safety parameters with the open square FA* Appendix C: Preliminary Core Analysis",FPN-P9IX-006, ENEA (2009). 20, 35

[19] R. N. Lyon, *Liquid-Metals Handbook*, 2nd ed., Atomic Energy Comm., Washington D.C. (1952) 37

[20] OECD/NEA, *Handbook on Lead-bismuth Eutectic Alloy and Lead Properties, Materials Compatibility, Thermal-hydraulics and Technologies*, OECD/NEA No. 6195, ISBN 978-92-64-99002-9 (2007) 37

[21] F. R. Menter, *Two-equation eddy-viscosity turbulence models for engineering applications*, AIAA J, 32, pp.269-289 (1994). 12

[22] D.C. Wilcox, *Re-assessment of the scale-determining equation for advanced turbulence models*, AIAA Journal, vol. 26, no. 11, pp. 1299-1310 (1988). 12

[23] D.C. Wilcox, *Turbulence Modeling for CFD*, ISBN 1-928729-10-X, 2nd Ed., DCW Industries Inc. (2004). 12

[24] Fluent Inc., *FLUENT 6.3 User's Guide*, Fluent Incorporated, USA (2006). 12

[25] MPI (Message Passing Interface) forum, http://www.mpi-forum.org/ 10

[26] OpenMPI library, http://www.open-mpi.org/ 10

[27] *PARAVIEW visualization software*, Official documentation at http://www.paraview.org 22

[28] PETSc (Portable Extension Toolkit for Scientific Computation), http://www.mcs.anl.gov/petsc/petsc-as/ 10

[29] CEA/DEN, *SALOME Documentation*, CEA/DEN, EDF R&D, OPEN CASCADE (2007-2008). 9

[30] *VTK library*, http://www.vtk.org 22

[31] LASPACK (Linear Algebra Sparse Matrix Package): http://www.mgnet.org/mgnet/Codes/laspack/html/laspack.html 10

[32] LIBMESH package: http://libmesh.sourceforge.net/ 10